# Atomic Force Microscopy (AFM) and its Applications to Bone-related Research

Yuxiao Zhou[a,b], Jing Du[a*]

[a] Department of Mechanical Engineering, Pennsylvania State University, University Park, PA

[b] Department of Mechanical Engineering, Texas A&M University, College Station, TX

* Correspondence to: Professor Jing Du

316B Leonhard Building

Penn State University

University Park, PA 16802

Phone: (814) 863-1043

Email: jingdu@psu.edu

Other authors:

Yuxiao Zhou yyz5239@psu.edu

**Abstract**

Bone consists of organic (mostly collagen) and inorganic (mostly bioapatite mineral) components that are organized into hierarchical structures from nano- to macro-scales that provide load-bearing functions. The structures and properties of bone are affected by bone remodeling activities, which are affected by mechanotransduction, a process through which mechanical signals are converted to biochemical signals in cellular signaling. Atomic Force Microscopy (AFM) technique can be used to characterize the surface morphology and mechanical properties of the specimens and can achieve atomic resolution in the resulting images. Therefore, the AFM technique has been applied in bone research and has provided new understandings of the structures and properties of hierarchical structures in bone across multiple length scales. This review begins by introducing the tip-surface interactions and the operation modes of AFM, including the recently developed sub-resonance modes, including PeakForce Tapping mode. Then the contact adhesion theories that have been used in analyzing AFM data are reviewed. It is followed by a systematic review of the applications of the AFM technique to bone and bone-related tissues and cells, including surface morphology imaging, contact indentation testing, and other mechanical tests. The applications of sub-resonance tapping mode to bone and other biological molecules, cells, and tissues are also reviewed.

Keywords: Atomic force microscopy (AFM), bone, surface morphology, mechanical properties, sub-resonance tapping.

## 1. Introduction

Atomic force microscopy (AFM) is a type of scanning probe microscopy (SPM). It interacts with testing samples using a probe that consists of a cantilever with a tip at its end. When the probe is brought into the proximity of the specimen, the interaction forces between the probe and the surface of the specimen cause deflection of the cantilever. Hence, AFM can be used to measure the surface morphology and properties of the specimens. The radius of the tip of the AFM probe can be in the order of nanometers. When the probe scans through the surface of the specimens, the resulting images can achieve atomic resolution (Giessibl, 1995).

Since its debut in 1986 (Binnig et al., 1986), there has been growing interest in using AFM as a material characterization method. It has contributed to extending our understanding of a wide range of hard and soft tissues. Specifically, there has been a growing interest in using AFM to study bone (Fig. 1). Because AFM can provide images and perform testing with high spatial resolution, it has been used to visualize the morphology and measure the mechanical properties of various structures in bone across multiple length scales.

Bone is a mineralized biological tissue that exhibits superior mechanical properties for its load-bearing functions (Fratzl et al., 2004). It is strong, tough, yet lightweight, which can be attributed to its hierarchical structures (Huang et al., 2019). A schematic in Fig. 2 presents the structures of bone across multiple length scales. Cortical bone is the dense outer surface of bone, that mainly consists of osteons. Trabecular bone is the porous bone that is composed of trabeculae, including plates and rods. On the micro-scale, lamellar structures exist in both osteons and trabeculae, with the boundaries marked by cement lines. At the nano-scale, the ultrastructure of bone consists of interwinding collagen fibrils and bioapatite mineral crystals. AFM has been used to investigate the morphology and properties of cortical bone, trabecular bone, bone lamellae,

cement lines, and mineralized collagen fibrils. The knowledge of the multiscale composition-structure-properties relationship of bone can lay the foundation for the development of bio-inspired materials with superior properties (Huang et al., 2019; Meza et al., 2015; Wegst et al., 2015).

Bone is a living tissue that continually renews itself through remodeling activities. The structure and properties of bone are affected by aging, diseases, and therapeutic treatments. AFM-related techniques have been used to study the changes in the structure and properties of bone due to these factors. Bone adaptation to mechanical loads (Currey, 2003) is a long-standing consensus since Wolff's law (Wolff, 1986) and Frost's mechanostat theory (Frost, 1994). Bone remodeling takes place in basic multicellular units (BMU) that include osteoclasts, osteoblasts, and osteocytes. It is a net result of continuous cycles of bone resorption by osteoclasts and formation by osteoblasts. Osteocytes are generally believed to be the regulator of osteoblasts and osteoclasts to accommodate mechanical loading and repair fatigue damage. They reside in lacunae, small cavities between the lamellae (Fig. 2). The lacunae are connected by canalicular, a network of sub-micron scale tunnels. Using AFM techniques, the structure and properties of lacunar-canalicular network in bone has also been investigated (Knapp et al., 2002)(Reilly et al., 2001)(Lin and Xu, 2011)(Zhang et al., 2015). These are useful for the understanding of mechanotransduction, a process through which mechanical signals are converted to biochemical signals in cellular signaling.

In this review, the commonly used operation modes of AFM for bone research are introduced, followed by the introduction of interactions between the tip of the AFM cantilever probe and the surfaces of the specimens. Next, several mechanical theories that have been used to analyze the force-separation curves obtained during AFM scanning to obtain mechanical properties of the substrates are reviewed, including the elastic contact models, the elastic-plastic indentation models,

and the adhesion models. Last, various applications of the AFM technique to bone and bone-related tissues and cells are reviewed, including the imaging of surface morphology and the measurement of mechanical properties of several structures in bone across multiple length scales. The applications of a recently developed AFM mode, the sub-resonance tapping mode, to bone and other biological molecules, cells, and tissues are also reviewed.

## 2. Operation of AFM

### 2.1 AFM Modes for Imaging

AFM can be operated in several different modes for various applications. The operating modes that are most commonly used in imaging the surface morphology of bone and other bone-related materials are contact mode and tapping mode.

Contact mode is the first AFM imaging mode, which was developed by Binnig, Quate, and Gerber in 1986 (Binnig et al., 1986). In contact mode, the AFM probe is lowered, usually by a piezoelectric actuator (Z-piezo), so that the tip is in continuous contact with the specimen while it scans through the surface of the specimen (XY-plane) pixel-by-pixel. Changes in the surface morphology of specimens result in cantilever deflection of the probe and deformation of the specimen. The contact mode can be operated in constant force mode in which the cantilever deflection (i.e. the force applied on the tip) is kept constant or in constant height mode in which the probe maintains at a fixed height above the specimen. An obvious drawback of contact mode is that sometimes the lateral force can be large. This may cause tip contamination by soft specimens, tip wearing by hard specimens, or specimen damage.

The tapping mode was later developed in 1993 (Zhong et al., 1993) and is currently the most popular AFM imaging mode. In tapping mode, the cantilever of the probe oscillates in the vertical

direction (Z-direction) at or near its resonance frequency so that the AFM tip taps the specimen lightly. Usually, the height of the probe is adjusted to keep the oscillation amplitude constant. In tapping mode, the friction and shear force on AFM tips are reduced to a negligible level, hence tapping mode is suitable for fragile samples. However, the resonant behavior of the probe makes it difficult to obtain the mechanical properties of the specimens from the data.

## 2.2 AFM Modes for Force Measurement and Mechanical Mapping

AFM can also be used to measure the mechanical proprieties of the specimens through the analysis of the interactions between the AFM tip and the surface of the specimen. The commonly used AFM modes for force measurement and mechanical mapping in bone-related research include the above-mentioned contact mode and force-volume mapping. In contact mode, the AFM tip can interact with the specimens at single points on specimens. In force-volume mapping, the AFM tip interacts with the specimens on a defined array of points on the specimen, and the tip-surface interaction within the defined volume is obtained. In these tests, AFM cantilever probes with different tips can be used, such as spherical (colloidal), conical, and Berkovich (pyramidal) tips. The tip-surface interactions can be analyzed to obtain materials properties, such as elastic modulus and adhesion energy, using contact, adhesion, or indentation theories, depending on the assumptions of elastic deformation, adhesion, or elastic-plastic deformation.

AFM equipment can also be combined with the nanoindentation apparatus to perform nanoindentation using stiff vertical metal probes with a diamond tip. The force-displacement data are recorded in the nanoindentation mode. The topology of the specimen can be obtained in contact or tapping AFM mode before the indentation to measure the surface roughness of the specimen and after the indentation to examine the indents left in the specimen and plastic flows in the substrate materials.

Sub-resonance AFM mode is a recently developed AFM mode for nanomechanical mapping (Su et al., 2014). It can have different names for different AFM manufacturers, for example PeakForce Tapping mode, pulsed force mode, HybriD, QI™ mode, AFM PinPoint™ nanomechanical mode. In sub-resonance mode, the vertical position of the probe (Z-piezo) is modulated at ~2 kHz; The cantilever oscillates at a frequency much lower than its resonance frequency; The tip taps the surface of the specimens. It allows fast scanning of the surface of the specimen to collect morphological information as well as to perform force measurements. Each tapping can be approximated as a quasi-static process. Force measurement is performed at every pixel location. The maximum normal force, i.e. peak force, during each tapping is controlled via a feedback loop and kept the same. The peak force is kept small so that the deformation of the specimen can be assumed to be within the elastic range. Another advantage of small peak force is that it can provide a high spatial resolution that is comparable to the spatial resolution for the tapping mode images (~5 nm). By using probes with different spring constants, in sub-resonance mode, the elastic modulus of the specimen in a wide range of 1 kPa to 100 GPa can be measured. Because the normal and lateral forces are both small during tapping, there is minimal damage to the probe and the sample.

### 2.3 Tip-surface Interactions

Using sub-resonance mode as an example, typical interactions between the AFM probe and the surface of the specimen during force measurement are summarized in Fig. 3. As the probe approaches the specimen, the tip experiences negligible interactions with the surrounding medium and the tip deflection remains close to zero (Fig. 3A). However, as the tip is lowered further down, it is eventually pulled into contact with the surface by adhesive force between the tip of the probe and the substrate (Fig. 3B). Subsequently, the probe continues to move down with the tip and

substrate in continuous contact. This causes the cantilever to bend under elastic deformation (Fig. 3C). Upon retraction, the probe is raised and its elastic deformation is reversed. However, residual adhesive interactions prevent the tip from detaching from the substrate at zero loads (Fig. 3D). Hence, the reversed loading of the tip must be continually increased until the adhesive forces are eventually overcome and the tip is pulled off from the substrate (Fig. 3E).

The vertical position of the probe is recorded. The deflection of the cantilever is measured, usually by measuring the laser beam reflection from the upper surface of the cantilever. The separation, i.e., the distance between the tip and the substrate is obtained by adding the vertical position to the cantilever deflection. When the separation is negative, it represents the deformation of the substrate, i.e., the indentation depth of the tip.

The force applied on the tip, $F$, can then be related to the deflection of the cantilever via Hooke's law. It is given by

$$F = k\Delta \qquad \text{(Eq. 1)}$$

where $k$ is the spring constant and $\Delta$ is the deflection of the cantilever, respectively. The spring constant of the compliant probes can be obtained through thermal tune (Hutter and Bechhoefer, 1998; Sarid et al., 1991). A typical force-separation relationship is presented in Fig. 3d.

## 3. AFM-related Mechanics Theories and Models

The force-separation curves obtained during AFM force measurements can be analyzed to obtain the mechanical properties of the substrate. Several related models and theories are reviewed in this section.

3.1 Contact Models

Assuming there are no adhesive surface forces, the elastic contact of two spheres under compressive load can be described by the classical Hertzian contact theory (Hertz, 1882). Assuming the materials of both spheres are homogeneous, isotropic, and linear elastic, and the radius of the contact area is much smaller than the radius of the two spheres, the contact radius, $a$, and the deformation of the two spheres (i.e. indentation depth), $\delta$, are given by

$$a = \left(\frac{3FR}{4E}\right)^{1/3} \quad \text{(Eq. 2)}$$

$$\delta = \frac{a^2}{R} \quad \text{(Eq. 3)}$$

where $F$ is the load; $E$ is the combined Young's modulus given by $1/E = (1 - {\nu_1}^2)/E_1 + (1 - {\nu_2}^2)/E_2$, where $E_1$ and $E_2$ are the elastic modulus, and $\nu_1$ and $\nu_2$ are the Poisson's ratio of the two spheres, respectively; $R$ is the combined radius given by $1/R = 1/R_1 + 1/R_2$, where $R_1$ and $R_2$ are the radius of the two spheres, respectively. A special case for Hertzian contact is the contact between a sphere and a half-space, of which the radius can be considered infinite.

In 1965, Sneddon (Sneddon, 1965) came up with a theoretical model that applies to the elastic half-space indented by a rigid axisymmetric punch. One of the special cases is a punch with a conical shape. This model relates the load, $F$, the contact radius, $a$, and the indentation, $\delta$, by

$$F = \frac{\pi E_s a^2}{2(1-{\nu_s}^2)} \tan\alpha \quad \text{(Eq. 4)}$$

$$\delta = \frac{1}{2}\pi a \tan\alpha \quad \text{(Eq. 5)}$$

where $E_s$ and $\nu_s$ denotes the elastic modulus and the Poisson ratio of the half-space, respectively; $\alpha$ is the semi-vertical angle of the cone.

The above-mentioned models are often used to analyze the force-separation curves obtained in AFM force measurements to obtain the elastic modulus of the specimen. While Hertzian contact theory is valid for spherical tips, the Sneddon model further extend it to other axisymmetric tip geometries. Both theories are valid under the condition that indentation depth is much smaller than tip radius. The deformation/indentation can be extracted from the force-separation curves. The substrate is often assumed to be flat. The geometry of the probe can be obtained through calibration on standard specimens with known Young's modulus, scanning through a substrate with sharp-edged structures, or direct measurement using scanning electron microscopy (SEM).

### 3.2 Contact Adhesion Theories

The adhesion force between the AFM tip and the substrate can be extracted from the force-separation curves obtained from AFM force measurements. Several prior theories have been proposed for the characterization of the contact adhesive interactions between two elastic spheres. The adhesion energy between the AFM tip and the substrate can be calculated by using these theories.

For realistic interactions, the integral of the force-distance attractive well, for example, Lennard-Jones potential, corresponds to the work of adhesion, i.e. adhesion energy, $\gamma$. The negative critical load at which the surfaces of two spheres separate, when being pulled apart, was defined as pull-off force or adhesion force.

In the cases when the adhesion forces are short-range compared to the elastic deformation that they produce (i.e. compliant material, strong adhesion, large radii), the Johnson-Kendall-Roberts (JKR) model applies (Johnson et al., 1971). The interaction force can be described by a delta function with adhesion strength, $\gamma$, and a short-range contact zone. This model relates the load, $F$, the contact radius, $a$, the indentation, $\delta$, and the adhesion force, $F_{ad}$, by

$$a = \left(\frac{3R}{4E}(F + 3\pi\gamma R + (6\pi\gamma RF + (3\pi\gamma R)^2)^{1/2})\right)^{1/3} \quad \text{(Eq. 6)}$$

$$\delta = \frac{a^2}{R} - (\frac{2\pi\gamma a}{E})^{1/2} \quad \text{(Eq. 7)}$$

$$F_{ad} = \frac{3}{2}\pi\gamma R \quad \text{(Eq. 8)}$$

where $E$ and $R$ are the combined Young's modulus and combined radius, respectively.

In contrast, the Derjaguin-Muller-Toporov (DMT) model (Derjaguin, 1975) describes a long-range surface force. It results in a Hertzian contact profile, with an additional external load as attractive forces (i.e. stiff materials, weak adhesion, small radii). The indentation, $\delta$, is given by the same equation in the Hertzian model (Equation 3). The contact radius, $a$, and the adhesion force, $F_{ad}$, are given by

$$a = \left(\frac{3R}{4E}(F + 2\pi\gamma R)\right)^{1/3} \quad \text{(Eq. 9)}$$

$$F_{ad} = 2\pi\gamma R \quad \text{(Eq. 10)}$$

Intermediate between the JKR and DMT models, the Maugis-Dugdale (MD) model (Maugis, 1992) proposes an analytical solution. To select the appropriate model, Maugis (Maugis, 1992) defined a transition parameter, λ. The JKR model applies when λ > 5. The DMT model applies when λ < 0.1. The MD model applies for the intermediate values of λ. Maugis (Maugis, 1992) used a Dugdale square well potential to approximate the interaction potential in reality. In this interaction, a constant adhesive stress $\sigma_0$ acts between the surfaces over a range of $\delta_t$. Thus, the work of adhesion, i.e. adhesion energy, can be calculated as $\gamma = \sigma_0\delta_t$. In the MD model, two equations are needed to relate the contact radius, $a$, and the applied load, $F$. However, the equations are difficult to use, since there is not a single expression relating only $a$ and $F$. The equations need to be solved simultaneously. Furthermore, in the usual case with experimental

measurements, such as AFM force measurement, the value of λ is unknown. The adhesion force must be determined through an iterative technique (Lantz et al., 1997).

Carpick et al. proposed another transition parameter, $\alpha$, and proposed a conversion equation from $\alpha$ to λ by curve fitting (Carpick et al., 1999). The equation for conversion was later modified by Pietrement and Troyon (Piétrement and Troyon, 2000). They also determined empirical equations supplying direct conversion equations between parameter $\alpha$, adhesion force, and adhesion energy (Piétrement and Troyon, 2000).

### 3.3 Elastic-Plastic Indentation

Oliver and Pharr contributed to understanding the mechanics governing elastic-plastic indentation, in which the unloading curve does not follow the loading curve because of the occurrence of plasticity. They provided a method to estimate material properties using the unloading curve in the indentation experiments, upon which the elastic deformation is recovered (Oliver and Pharr, 1992). The contact stiffness, $S$, of the upper portion of the unloading curve is given by

$$S = \frac{2}{\sqrt{\pi}} E_r \sqrt{A} \qquad \text{(Eq. 11)}$$

where $A$ is the contact area, and $E_r$ is the reduced modulus. The reduced modulus, $E_r$, is defined by $1/E_r = (1 - {\nu_i}^2)/E_i + (1 - {\nu_s}^2)/E_s$, where $E_i$ and $E_s$ are the elastic modulus, and $\nu_i$ and $\nu_s$ are the Poisson's ratio of the indenter and the substrate, respectively. The contact area, $A$, depends on the geometry of the indenter.

This model is often used to analyze the data collected in elastic-plastic indentation experiments. The contact stiffness can be experimentally determined through the analysis of the unloading part of the load-displacement curve. The contact area as a function of contact depth can

be determined through calibration on standard specimens with known Young's modulus. With the material properties of the tip being known, the material properties of the substrate can be determined.

## 4. Application of AFM to bone-related research

Various applications of AFM techniques to bone-related research are reviewed in this section. Based on the different modes of AFM and its different applications, this section is divided into several subsections, staring from the first developed imaging modes, expanding to the later developed force measurement modes, and ending with the recent advances in sub-resonance tapping mode. In each subsection, generally, the literatures are organized in chronological order. Usually, the applications of AFM on native bone and components of bone (osteons, lamellae, collagens, minerals, lacunae, canaliculi) are reviewed; Then the effects of aging, disease, specimen preparation, and testing environment are discussed; Last, selected applications of AFM on bone-related tissues (tendon and cartilage) are also briefly introduced. Thus, the development of the AFM techniques and the improvement of the understanding of bone are presented. In particular, the elastic modulus of bone and some components in bone that were measured using various AFM methods are summarized in Table 1.

### 4.1 Surface Morphology

In 1992, Tao et al. used contact mode AFM with constant force to image the surface of a section of hydrated cow tibia. The results showed the concentric structure of micro-scale osteonal lamellae (Tao et al., 1992). Later, using tapping mode AFM (Xu et al., 2003), Xu et al. also showed the lamellar structures in the osteons in human cortical bone, including the thick and thin sub-lamellae (Fig. 4a).

The minerals isolated from bovine bone have been scanned by tapping mode AFM since 2001 (Eppell et al., 2001; Tong et al., 2003). The results show that isolated minerals were small platelets with an average size of ~10 nm and an average thickness of 0.61 or 2 nm. Since 2002, without isolation, the morphology of the minerals in bone has been characterized using AFM under either tapping or contact mode (Fig. 4b). The size of these minerals ranged from 20 nm to 200 nm, with a thickness of 5 nm (Hassenkam et al., 2004; Knapp et al., 2002; Sasaki et al., 2002) (Fig. 4b). A 2011 study showed that the size of the minerals in the trabeculae, measured by tapping mode AFM, for elderly women (73– 94 years) was greater than that for the younger women (20–40 years) (Milovanovic et al., 2011).

The morphology of the Type I collagen fibrils or fibril bundles in bone was also measured using AFM under either tapping or contact mode. In 2001, Thalhammer et al. showed that the diameter of collagen fibril bundles in the human femoral bone was about 400 nm (Thalhammer et al., 2001). AFM has also been used to measure the diameter and D-spacing (period) of single collagen fibrils in sheep tibiae (Fig. 4c) (Knapp et al., 2002), in bovine femora (Sasaki et al., 2002), in the trabecular bone in bovine vertebrae (Hassenkam et al., 2004), and in the resorption pits in bovine cortical bone (Bozec et al., 2005). The diameter of the collagen fibrils was measured to be 110 nm (Sasaki et al., 2002) and 62 nm (Bozec et al., 2005), and the D-spacing was measured to be 67 nm (Bozec et al., 2005; Hassenkam et al., 2004; Sasaki et al., 2002). Further studies showed that the morphology of the mineralized collagen fibrils in bone could be affected by elevated temperature in boiling or baking (Fantner et al., 2004), chemical treatment (Ge et al., 2007; Kindt et al., 2007), estrogen depletion (Wallace et al., 2010), or osteogenesis imperfecta (Wallace et al., 2011). These changes can affect mechanical behaviors, especially the fracture behaviors of bone (Fantner et al., 2004; Wallace et al., 2011, 2010).

AFM was also used to investigate the surface morphology and dimensions of the lacunar-canalicular network. The results indicated that the walls of canaliculi were lined with collagen fibrils arranged in parallel (Knapp et al., 2002)(Reilly et al., 2001). The width and height of the cross-sections of canaliculi (Reilly et al., 2001) (Lin and Xu, 2011), the spacing between canaliculi (Lin and Xu, 2011), and the dimensions of lacunae (Lin and Xu, 2011) were measured by AFM imaging (Fig. 4d). The morphology of living osteoblasts has been characterized by AFM as well to test the biocompatibility of implant materials (Domke et al., 2000). The surface morphology of the resorption pits on trabecular bone samples (Hassenkam et al., 2006) and dentin slices (Sasaki et al., 1993) as a result of osteoclasts culturing has also been characterized by AFM.

The morphology of other tissues connecting to the bone has also been characterized by AFM, including the morphology of collagen in rat tail tendons (Raspanti et al., 2001) and bovine Achilles tendons (Yang et al., 2008) and the height of the aggrecan molecule layer in cartilages (Dean et al., 2005).

4.2 Mechanical Testing: Nanoindentation

Since 1997, Pharr and Rho et al. have published a series of articles on using the nanoindentation technique and Oliver-Pharr model (Oliver and Pharr, 1992) to measure the elastic properties of bone. Though the nanoindentation device used was not coupled with AFM, these works pioneered the application of the nanoindentation technique in bone research. They measured the elastic modulus and hardness of osteon and interstitial bone in cortical bone, respectively, as well as trabecular bone, in dried human vertebrae and tibiae from different directions. The measured elastic modulus ranged from 13.5 to 25.8 GPa (Fan et al., 2002; J.-Y. Rho et al., 1999; J. Y. Rho et al., 1999; Rho et al., 1997; Roy et al., 1999). For each bone type, the elastic modulus and hardness of bone in the load-bearing direction were greater than those in the other directions

(Roy et al., 1999). For the completed secondary osteons, elastic modulus and hardness generally decreased from the center of the osteon outward (Rho et al., 1999). They developed theoretical models to derive the elastic constants for anisotropic materials from the nanoindentation data (Fan et al., 2002). Besides human bone, they have also studied bovine bone (Rho and Pharr, 1999), intramuscular herring bone (*Clupea harengus*) (Rho et al., 2001), and equine radius (Rho et al., 2001). They also found that the elastic modulus and hardness of dried cortical bone in bovine femurs were (9.7%–17.6%) higher than the bone stored in deionized water (Rho and Pharr, 1999).

When the nanoindentation apparatus, including the vertical stiff metal probe with a diamond tip, was combined with AFM equipment, the indentation modulus can be determined by the Oliver-Pharr method (Oliver and Pharr, 1992); the topology of the specimen before/after indentation can be obtained and the indent locations can be determined, which is useful for the characterization of heterogeneous materials, including bone. Using this technique, in 2002, Hengsberger et al. differentiated the indentation on thick and thin sub-lamellae (Fig. 5a) and showed that the indentation modulus of thick lamellae was higher than that of thin sub-lamellae under low indentation force (0.4 mN and 1 mN), which results in small indent size (Hengsberger et al., 2002). They attributed the difference to the compositional and/or ultrastructural differences between thick and thin sub-lamellae. Xu et al. showed that the topology and the elastic modulus of thick and thin sub-lamellae determined by this combined AFM and nanoindentation technique was affected by sample preparation techniques, microtome sectioning followed by diamond knife cutting, compared with diamond saw cutting followed by mechanical polishing (Xu et al., 2003). For the thick and thin sub-lamellae, the variation in height for microtomed specimens was smaller than that for the cut and polished specimens. However, the variation in the elastic modulus for microtomed specimens was greater than that for the cut and polished specimens. Donnelly et al.

applied this technique to the trabecular bone in rabbits (Fig. 5b). The indentation modulus measured on smooth specimens with shallow indents (500 μN indentation force) was 26.6 ± 2.27 GPa and 20.3 ± 2.09 GPa, respectively, for the thick and thin sub-lamellae (Donnelly et al., 2006). Using this technique, Carnelli et al. showed that the spatial distribution of indentation modulus in osteons in the bovine cortical bone along axial and transverse directions had a clear sinusoidal pattern, especially with shallow indents (50 nm indentation depth) (Fig. 5c and 5d) (Carnelli et al., 2013). Incorporated with analytical models, they attributed the anisotropic behaviors and variations in the modulus to the arrangement of underlying mineralized collagen fibrils.

This combined AFM and nanoindentation technique has also been used to study the effects of gene mutation on the mechanical properties of skeletal bone for Zebrafish (*Danio rerio*) (Zhang et al., 2002). In another study, bovine tibial cortical bone was partly and completely demineralized by ethylenediaminetetraacetic acid (EDTA). And, the combined AFM and nanoindentation technique was applied to compare the effects of mineral content on the mechanical properties and deformation mechanisms of bone (Tai et al., 2005).

Besides the above-mentioned static testing, the testing can also be performed in dynamic loading mode. Asif et al. developed nanoscale Dynamic Mechanical Analysis (DMA) using the direct force modulation mode of a nanoindenter mounted on an AFM (Syed Asif et al., 2001, 1999). This technique has been used to map the elastic modulus in mice cortical mid-tibia (Balooch et al., 2005). The results showed heterogeneity in the elastic modulus map for D4 mice, a phenotype to study TGF-β signaling, but not for the wild-type mice (Balooch et al., 2005).

### 4.3 Mechanical Testing: Contact Indentation

Contact indentation can also be performed using AFM cantilever probes, which are more flexible than vertical metal nanoindentation probes. Compared with stiff nanoindentation probes,

the flexible AFM cantilever probe applies lower indentation force, results in shallower indentation depth and smaller indent size, and can be used to conduct indentations with smaller spacing. Depending on the elastic or elastic-plastic assumptions, Hertz/Sneddon model or Oliver-Pharr theories can be used to analyze the force-separation data and to derive the elastic modulus.

In an attempt to measure the rigidity modulus of the lamellae in the osteons and the interstitial bone, In 1992, Tao et al. analyzed the force-separation data that were obtained during AFM contact mode measurements on bovine tibia using Sneddon's model (Tao et al., 1992). In 2000, Domke et al. used force mapping mode AFM and the Sneddon model to obtain the elastic property map of living osteoblasts and contact mode AFM to examine their morphology (Fig.6). The results showed linearly patterned structures in the cytoskeleton, presumably stress fibers, i.e. bundles of actin filaments. They were with intermediate values of Young's modulus and laid all over the cell. They compared the osteoclasts on metallic substrates and on glass and tissue culture polystyrene to test the biocompatibility of implant materials (Domke et al., 2000).

In 2007, Tai et al. conducted indentation on bone using AFM probes and analyzed the results using the Oliver-Pharr method (Tai et al., 2007). The work was later extended by Yao et al. to be compared with the results obtained using conventional nanoindentation with stiff vertical metal probes (Yao et al., 2011). Their results show that using AFM probe indentation, with a spatial resolution below 200 nm, the elastic modulus of bone is not uniform (Fig. 7). In contrast, the heterogeneity in the elastic modulus was not very profound when using conventional nanoindentation, with a spatial resolution above 200 nm. They suggested that the size-dependent heterogeneity promotes energy dissipation at the nanoscale, but suppresses stress concentration and strain localization at larger length scales, hence it is beneficial for the mechanical behaviors of bone (Yao et al., 2011).

The morphology and mechanical properties of collagen fibrils have also been investigated using AFM. Wenger et al. used force mapping AFM and Oliver-Pharr method and obtained an elastic modulus of 5 to 11.5 GPa for Type I collagen fibrils dissected from rat tail tendons in air at room temperature (Wenger et al., 2007). Balooch et al. used the Sneddon model to analyze the force-displacement curves obtained through the indentation test performed by AFM cantilever probes. The elastic modulus was measured to decrease from 1.5 GPa to 50 MPa during demineralization for mineralized collagen fibrils in human dentin (Balooch et al., 2008). Gaidash et al. used contact mode AFM to characterize the adhesion forces on collagen fibrils in rat bone (Gaidash et al., 2011).

Besides bone, the contact indentation type AFM has also been applied to other bone-related tissues. In 2004, Stolz et al. applied this technique to porcine articular cartilage and used the Oliver-Pharr method to obtain its elastic modulus (Stolz et al., 2004). In the same year, Allen and Mao applied a similar technique to rat synchondrosis and used the Hertz model to obtain its elastic modulus (Allen and Mao, 2004). The contact indentation type AFM combined with the Hertz model has then been applied by many other researchers to characterize the elastic modulus of various cartilages (Chandrasekaran et al., 2017; Darling et al., 2010; Kwok et al., 2014; Li et al., 2015; Roddy et al., 2011; Wilusz et al., 2012). The measured elastic modulus ranged from several kPa to several MPa. The contact indentation type AFM has also been used to measure the viscoelastic properties of cartilage by holding the AFM cantilever probe at a constant displacement for the stress-relaxation test and modifying the Hertz model with viscoelastic equations (Darling et al., 2006). The elastic modulus and morphology of tendons have also been characterized using contact indentation type AFM and the Hertz model (Marturano et al., 2013)(Lozano et al., 2019). The above-mentioned AFM contact indentation testing was performed under the static loading

condition. Campbell et al. demonstrated that a dynamic AFM method, contact resonance force microscopy, can be used to quantitatively map the viscoelastic properties in the cartilages in a femoral head of a New Zealand white rabbit (Campbell et al., 2012).

### 4.4 Mechanical Testing: Tension and Bending

In 2001, Hansma and collaborators performed AFM force measurements on collagen samples prepared from acid-insoluble collagens from bovine Achilles tendons, as well as on the cut and polished rat femur specimens (Thompson et al., 2001). They suggested that some molecules were attached to the AFM tip when the probe was brought into the proximity of the specimens. They were then pulled when the probe was retracted. The traction-separation curves recorded during retraction were analyzed as load-displacement curves for the tension of these molecules. They exhibited multiple discontinuities, for both tests on collagen and bone specimens. Graham et al. observed similar discontinuity patterns in the traction-separation curves in the AFM tension test of collagens and attributed them to the reorganization within the fibrils (Graham et al., 2004). Later in 2005, Hansma and collaborators performed AFM force measurements on bone with another piece of bone glued to the AFM probe. It resulted in traction-separation curves with similar discontinuity patterns during retraction (Fig. 8b) (Fantner et al., 2005). Supported by the SEM images and AFM images (Fig. 8a), they attributed the discontinuities to the effects of the non-fibrillar organic matrix in bone, which acts as an adhesive material that holds the mineralized collagen fibrils together.

In 2006, van der Rijt et al. performed tensile tests of single collagen fibrils from the bovine Achilles tendon, with the collagen fibrils glued to the AFM tip and the substrate, confirmed by optical and electron microscopes (Fig. 8c). The stress-strain curves did not exhibit obvious discontinuities (Fig. 8d) and Young's modulus was measured to be 2–7 GPa in ambient conditions

and 0.2–0.5 GPa in phosphate-buffered saline (PBS) solution (van der Rijt et al., 2006). Similar results were obtained from similar tests that were performed by other groups on single collagen fibrils from human patellar tendon fascicles (Svensson et al., 2010) and the antler of a deer (Hang and Barber, 2011) with the fibrils glued with the assistance of an optical or electronic microscope. The results also showed rate-dependent tensile behaviors of the collagen fibrils (Svensson et al., 2010).

In 2008, Yang et al. performed bending tests of collagen fibrils from the bovine Achilles tendon (Yang et al., 2008). Collagen fibrils were spanned across microscale channels in the glass substrates and scanned using tipless AFM probes. The measured bending moduli ranged from 1.0–3.9 GPa at ambient conditions and 0.07–0.17 GPa in PBS solution. In 2012, Jimenez-Palomar et al. performed bending tests of microscale beams of rat femur fabricated by focused ion beam (FIB) milling using *in situ* AFM coupled with SEM (Jimenez-Palomar et al., 2012). Guided by SEM, AFM probes were used to apply bending force on the microscale beam-shaped bone specimens. Using similar techniques, tension tests have also been performed on the microscale beam-shape specimens fabricated from tendon-to-bone attachment sites in mice humeral heads (Deymier et al., 2017).

### 4.5 Recent Advances with Sub-Resonance Tapping AFM

Since 2011, sub-resonance tapping AFM mode has been used to characterize the topography and the mechanical properties of soft and hard biological molecules, cells, and tissues with elastic modulus ranging from several kPa to a few dozen GPa. Most work have been applications on soft tissues, cells and molecules.

PeakForce AFM has been used to study biological molecules, including the topology and stiffness of bacteriorhodopsin, a transmembrane protein (Rico et al., 2011). The resulting images

were of sub-molecular resolution. The stiffness of the sample was determined by the slope of the force-separation curve where the tip and substrate were in contact. PeakForce AFM has also been used to investigate single human immunoglobulin G and M antibodies in liquid (Voss et al., 2015). The results showed ultrastructural details of these molecules with sub 10 nm resolution and an elastic modulus of 34 MPa. Adhesion force maps were also obtained at the same time. Additionally, this technique has been used to investigate the morphology and mechanical properties of amyloid fibrils (Adamcik et al., 2011). The results showed that the fibrils had an average height of 2.5 nm and an elastic modulus of 3.7 GPa.

PeakForce AFM has been used to map the topography and elastic modulus inside individual cells, including human epidermal cells (Heu et al., 2012), and living breast cancer cells (Calzado-Martín et al., 2016), and murine and rat fibroblast cells (Efremov et al., 2019), with elastic modulus ranging from 0.2 to 300 kPa. Efremov et al. compared the elastic and viscoelastic properties of fibroblast cells measured using fast force volume mode and PeakForce Tapping mode. Using Ting's model for indentation on viscoelastic materials and the power-law rheology model for the viscoelastic behaviors, both AFM modes have provided self-consistent results (Efremov et al., 2019). Besides elastic and viscoelastic properties, the hydrophobicity of live cells and the adhesion of single proteins on living yeast cells have been studied by using PeakForce AFM with chemically functionalized tips (Alsteens et al., 2012).

The challenges of applying sub-resonance tapping AFM on hard tissues and materials come from several aspects. The AFM probe has to be carefully selected to have a spring constant that is high enough for hard materials. Since thermal tuning method may not work well for stiff cantilevers, other methods need to be explored for the calibration of the cantilever stiffness. Controlling the testing environment is also important. Water will affect the microstructure and

mechanical properties of hard tissues, especially the organic components. Water will also bring some challenges for the vibration of stiff probes.

To the best of our knowledge, currently, there are limited journal articles on the application of sub-resonance mode AFM to bone research. In the earliest one, Zhang et al. used PeakForce quantitative nanomechanical mapping (QNM) to investigate the mechanical properties of the lacunar-canalicular network surrounding osteocytes in the cortical bone in rat femur (Zhang et al., 2015). Their results show that the elastic modulus determined by PeakForce AFM was of the same magnitude as that obtained using the nanoindentation technique. However, PeakForce AFM provided higher spatial resolution than nanoindentation and allowed the study of micro- and nano-structures in bone. They suggested that the reduced elastic modulus of the perilacunar matrix (10.0 ± 2.8 GPa) was much lower than that of the bone matrix (28.8 ± 10.1 GPa) (Figs. 9abc), and the reduced elastic modulus of the pericanalicular matrix (20.0 ± 7.5 GPa) was also significantly lower than that of the bone matrix (31.6 ± 5.2 GPa) (Figs. 9def). They also measured the reduced elastic modulus of collagen fibers embedded in the perilacunar matrix to be 12.6 ± 3.5 GPa (Figs. 9ghi).

In a later work, Zhang et al. evaluated the nanostructure and nanomechanics of newly-formed bone in the defect center treated with biomimetic intrafibrillarly-mineralized collagen (IMC) and hydroxyapatite (HA) scaffolds, respectively, using PeakForce QNM mode (Zhang et al., 2017). The surface morphology map and the Young's modulus map were presented. The average and standard deviation of the Young's modulus were reported. Moreover, Asgari et al. conducted a thorough study on the material anisotropy and elasticity of cortical and trabecular bone in the adult mouse femur using an AFM-based indentation with an indentation frequency between 1 and 500 Hz (Asgari et al., 2019). The method is comparable to the PeakForce tapping mode AFM. The

elastic modulus was measured in cortical and trabecular bone, from longitudinal and transverse directions, at different locations and different indentation frequencies, respectively.

Our group has used PeakForce QNM mode to map the morphology and elastic modulus map of several structures across multiple length scales in the cortical bone in bovine femurs (Zhou et al., 2020). The specimens were fully submerged in DI water during testing to create a near-physiological testing environment. In the sub-millimeter scale, the elastic modulus of osteons (20.51 ± 6.85 GPa) was measured to be slightly lower than the interstitial bone (21.87 ± 5.48 GPa). In the microscale, the elastic modulus in the lamellar structures in an osteon varied periodically from higher values in thick sub-lamellae (21.49 ± 6.58 GPa) to lower values in thin sub-lamellae (9.67 ± 2.69 GPa) (Fig. 10a). The elastic modulus of thin sub-lamellae was lower than that measured using the nanoindentation technique (section 4.3), which can be attributed to the higher spatial resolution offered by PeakForce AFM than that for nanoindentation. The histogram of elastic modulus contained three dominating peaks for the thick and thin sub-lamellae, respectively, indicating the underlying fiber orientations (Fig. 10bc). The elastic modulus of another structure on the microscale, the cement lines, was also measured (7.49 ± 4.23 GPa). Cement lines play an important role in the fracture and fatigue behaviors of bone and this was the first time that its elastic modulus was experimentally determined. The results also showed relatively softer mineralized collagen fibril bundle arrays (12.94 ± 2.71GPa) embedded in harder extrafibrillar matrix materials (28.39 ± 5.75 GPa), which shed light on the ultrastructure of bone (Fig. 10de). The histogram of the elastic modulus of the collagen fibril bundles was mostly dominated by one general normal distribution, which suggested one dominating angle between the fibrils and the AFM tapping direction, i.e. the long axis of the bone (Fig. 10f). It was consistent with the ultrastructure model, in which the collagen fibrils and mineral particles weaved together like a

twisting rope (Reznikov et al., 2014a). In contrast, there were multiple peaks in the histogram of the elastic modulus of the extrafibrillar matrix (Fig. 10g). It was attributed to the random orientations of fibrils, the substantial ground substance, and the sub-micron voids in the disordered extrafibrillar matrix (Reznikov et al., 2014b).

Using sub-resonance mode AFM, the surface topography of wear particles and human knee cartilage were characterized and the elastic modulus was measured to be from ~5 to 25 MPa for wear particles found in healthy and osteoarthritic knee joints (Wang and Peng, 2015). By applying sub-resonance mode AFM, the elastic modulus of corneal stroma has been measured to be reduced from 7.10 GPa to 1.84 MPa with the increasing hydration level (Xia et al., 2014). Moreover, the elastic modulus of human cementum was measured by this technique to be 9.84 ± 5.13 GPa and 7.42 ± 2.39 GPa, respectively, for healthy and cathepsin K gene mutated dentin (Xue et al., 2015).

## 5. Summary

This review presents the operation modes, the theoretical background, and the applications of the atomic force microscope in bone and bone-related research. The emergence of AFM in 1986 and its expansion in operating modes have greatly improved our understanding of the structure and the mechanical properties of bone. AFM-related techniques have been used to image the surface morphology and to measure the mechanical properties of different types of bone, various structures in bone across multiple length scales, bone with and without diseases, and treatments. Recent advancement in the AFM technique, the sub-resonance mode AFM, allows fast mapping of the morphology and mechanical properties of bone. In the future, the applications of the AFM technique will further expand our understanding of bone and other natural materials.

## Conflict of Interest

We acknowledge that all authors do not have any conflict of interest and were fully involved in the preparation of the manuscript.


## Funding sources

This work is supported by the National Science Foundation under Grant Number DMR-2144614 and the Center of Biodevices at Penn State University through the Grace Woodward Award.

## Acknowledgment

The authors are grateful to the program managers, Dr. Nitsa Rosenzweig, Dr. Germano Iannacchione, and Dr. Steve Smith, for their encouragement and support. Appreciation is extended to Dr. Wole Soboyejo at Worcester Polytechnic Institute, Dr. Timothy Tighe, and Dr. Markus Kastner at Penn State MRI for useful technical discussions.


## Reference


Adamcik, J., Berquand, A., Mezzenga, R., 2011. Single-step direct measurement of amyloid fibrils stiffness by peak force quantitative nanomechanical atomic force microscopy. Appl. Phys. Lett. 98, 193701. https://doi.org/10.1063/1.3589369

Allen, D.M., Mao, J.J., 2004. Heterogeneous nanostructural and nanoelastic properties of pericellular and interterritorial matrices of chondrocytes by atomic force microscopy. J. Struct. Biol. 145, 196–204. https://doi.org/10.1016/j.jsb.2003.10.003

Alsteens, D., Dupres, V., Yunus, S., Latgé, J.-P., Heinisch, J.J., Dufrêne, Y.F., 2012. High-Resolution Imaging of Chemical and Biological Sites on Living Cells Using Peak Force

Tapping Atomic Force Microscopy. Langmuir 28, 16738–16744. https://doi.org/10.1021/la303891j

Asgari, M., Abi-Rafeh, J., Hendy, G.N., Pasini, D., 2019. Material anisotropy and elasticity of cortical and trabecular bone in the adult mouse femur via AFM indentation. J. Mech. Behav. Biomed. Mater. 93, 81–92. https://doi.org/10.1016/j.jmbbm.2019.01.024

Balooch, G., Balooch, M., Nalla, R.K., Schilling, S., Filvaroff, E.H., Marshall, G.W., Marshall, S.J., Ritchie, R.O., Derynck, R., Alliston, T., 2005. TGF- regulates the mechanical properties and composition of bone matrix. Proc. Natl. Acad. Sci. 102, 18813–18818. https://doi.org/10.1073/pnas.0507417102

Balooch, M., Habelitz, S., Kinney, J.H., Marshall, S.J., Marshall, G.W., 2008. Mechanical properties of mineralized collagen fibrils as influenced by demineralization. J. Struct. Biol. 162, 404–410. https://doi.org/10.1016/j.jsb.2008.02.010

Binnig, G., Quate, C.F., Gerber, C., 1986. Atomic Force Microscope. Phys. Rev. Lett. 56, 930–933. https://doi.org/10.1103/PhysRevLett.56.930

Bozec, L., Groot, J. de, Odlyha, M., Nicholls, B., Nesbitt, S., Flanagan, A., Horton, M., 2005. Atomic force microscopy of collagen structure in bone and dentine revealed by osteoclastic resorption. Ultramicroscopy 105, 79–89. https://doi.org/10.1016/j.ultramic.2005.06.021

Calzado-Martín, A., Encinar, M., Tamayo, J., Calleja, M., San Paulo, A., 2016. Effect of Actin Organization on the Stiffness of Living Breast Cancer Cells Revealed by Peak-Force Modulation Atomic Force Microscopy. ACS Nano 10, 3365–3374. https://doi.org/10.1021/acsnano.5b07162

Campbell, S.E., Ferguson, V.L., Hurley, D.C., 2012. Nanomechanical mapping of the osteochondral interface with contact resonance force microscopy and nanoindentation. Acta Biomater. 8, 4389–4396. https://doi.org/10.1016/J.ACTBIO.2012.07.042

Carnelli, D., Vena, P., Dao, M., Ortiz, C., Contro, R., 2013. Orientation and size-dependent mechanical modulation within individual secondary osteons in cortical bone tissue. J. R. Soc. Interface 10, 20120953. https://doi.org/10.1098/rsif.2012.0953

Carpick, R., Ogletree, D., Salmeron, M., 1999. A general equation for fitting contact area and friction vs load measurements. J. Colloid Interface Sci. 211, 395–400. https://doi.org/10.1006/jcis.1998.6027

Chandrasekaran, P., Doyran, B., Li, Q., Han, B., Bechtold, T.E., Koyama, E., Lu, X.L., Han, L., 2017. Biomechanical properties of murine TMJ articular disc and condyle cartilage via AFM-nanoindentation. J. Biomech. 60, 134–141. https://doi.org/10.1016/j.jbiomech.2017.06.031

Currey, J.., 2003. The many adaptations of bone. J. Biomech. 36, 1487–1495. https://doi.org/10.1016/S0021-9290(03)00124-6

Darling, E.M., Wilusz, R.E., Bolognesi, M.P., Zauscher, S., Guilak, F., 2010. Spatial Mapping of the Biomechanical Properties of the Pericellular Matrix of Articular Cartilage Measured In Situ via Atomic Force Microscopy. Biophys. J. 98, 2848–2856. https://doi.org/10.1016/j.bpj.2010.03.037

Darling, E.M., Zauscher, S., Guilak, F., 2006. Viscoelastic properties of zonal articular chondrocytes measured by atomic force microscopy. Osteoarthr. Cartil. 14, 571–579. https://doi.org/10.1016/j.joca.2005.12.003

Dean, D., Han, L., Ortiz, C., Grodzinsky, A.J., 2005. Nanoscale Conformation and Compressibility of Cartilage Aggrecan Using Microcontact Printing and Atomic Force Microscopy. Macromolecules 38, 4047–4049. https://doi.org/10.1021/ma047626k

Derjaguin, B., 1975. Effect of contact deformations on the adhesion of particles. J. Colloid Interface Sci. 53, 314–326. https://doi.org/10.1016/0021-9797(75)90018-1

Deymier, A.C., An, Y., Boyle, J.J., Schwartz, A.G., Birman, V., Genin, G.M., Thomopoulos, S., Barber, A.H., 2017. Micro-mechanical properties of the tendon-to-bone attachment. Acta Biomater. 56, 25–35. https://doi.org/10.1016/j.actbio.2017.01.037

Domke, J., Dannöhl, S., Parak, W.J., Müller, O., Aicher, W.K., Radmacher, M., 2000. Substrate dependent differences in morphology and elasticity of living osteoblasts investigated by atomic force microscopy. Colloids Surfaces B Biointerfaces 19, 367–379. https://doi.org/10.1016/S0927-7765(00)00145-4

Donnelly, E., Baker, S.P., Boskey, A.L., van der Meulen, M.C.H., 2006. Effects of surface roughness and maximum load on the mechanical properties of cancellous bone measured by nanoindentation. J. Biomed. Mater. Res. Part A 77A, 426–435. https://doi.org/10.1002/jbm.a.30633

Efremov, Y.M., Shpichka, A.I., Kotova, S.L., Timashev, P.S., 2019. Viscoelastic mapping of cells based on fast force volume and PeakForce Tapping. Soft Matter 15, 5455–5463. https://doi.org/10.1039/C9SM00711C

Eppell, S.J., Tong, W., Katz, J.L., Kuhn, L., Glimcher, M.J., 2001. Shape and size of isolated bone mineralites measured using atomic force microscopy 6, 3–10.

Fan, Z., Swadener, J.G., Rho, J.Y., Roy, M.E., Pharr, G.M., 2002. Anisotropic properties of human tibial cortical bone as measured by nanoindentation. J. Orthop. Res. 20, 806–810. https://doi.org/10.1016/S0736-0266(01)00186-3

Fantner, G.E., Birkedal, H., Kindt, J.H., Hassenkam, T., Weaver, J.C., Cutroni, J.A., Bosma, B.L., Bawazer, L., Finch, M.M., Cidade, G.A.G., Morse, D.E., Stucky, G.D., Hansma, P.K., 2004. Influence of the degradation of the organic matrix on the microscopic fracture behavior of trabecular bone. Bone 35, 1013–1022. https://doi.org/10.1016/j.bone.2004.05.027

Fantner, G.E., Hassenkam, T., Kindt, J.H., Weaver, J.C., Birkedal, H., Pechenik, L., Cutroni, J.A., Cidade, G.A.G., Stucky, G.D., Morse, D.E., Hansma, P.K., 2005. Sacrificial bonds and hidden length dissipate energy as mineralized fibrils separate during bone fracture. Nat. Mater. 4, 612–616. https://doi.org/10.1038/nmat1428

Fratzl, P., Gupta, H.S., Paschalis, E.P., Roschger, P., 2004. Structure and mechanical quality of the collagen–mineral nano-composite in bone. J. Mater. Chem. 14, 2115–2123. https://doi.org/10.1039/B402005G

Frost, H.M., 1994. Wolff's Law and bone's structural adaptations to mechanical usage: an overview for clinicians.

Gaidash, A.A., Sinitsa, L.N., Babenko, O.A., Lugovskoy, A.A., 2011. Nanoporous Structure of Bone Matrix at Osteoporosis from Data of Atomic Force Microscopy and IR Spectroscopy. J. Osteoporos. 2011, 1–7. https://doi.org/10.4061/2011/162041

Ge, J., Cui, F.-Z., Wang, X., Wang, Y., 2007. New evidence of surface mineralization of collagen fibrils in wild type zebrafish skeleton by AFM and TEM. Mater. Sci. Eng. C 27,

46–50. https://doi.org/10.1016/j.msec.2006.01.006

Giessibl, F.J., 1995. Atomic Resolution of the Silicon (111)-(7×7) Surface by Atomic Force Microscopy. Science (80-. ). 267, 68–71. https://doi.org/10.1126/science.267.5194.68

Graham, J.S., Vomund, A.N., Phillips, C.L., Grandbois, M., 2004. Structural changes in human type I collagen fibrils investigated by force spectroscopy. Exp. Cell Res. 299, 335–342. https://doi.org/10.1016/j.yexcr.2004.05.022

Hang, F., Barber, A.H., 2011. Nano-mechanical properties of individual mineralized collagen fibrils from bone tissue. J. R. Soc. Interface 8, 500–505. https://doi.org/10.1098/rsif.2010.0413

Hassenkam, T., Fantner, G.E., Cutroni, J.A., Weaver, J.C., Morse, D.E., Hansma, P.K., 2004. High-resolution AFM imaging of intact and fractured trabecular bone. Bone 35, 4–10. https://doi.org/10.1016/j.bone.2004.02.024

Hassenkam, T., Jørgensen, H.L., Lauritzen, J.B., 2006. Mapping the imprint of bone remodeling by atomic force microscopy. Anat. Rec. Part A Discov. Mol. Cell. Evol. Biol. 288A, 1087–1094. https://doi.org/10.1002/ar.a.20376

Hengsberger, S., Kulik, A., Zysset, P., 2002. Nanoindentation discriminates the elastic properties of individual human bone lamellae under dry and physiological conditions. Bone 30, 178–184. https://doi.org/10.1016/S8756-3282(01)00624-X

Hertz, V.H.H., 1882. Ueber die Berührung fester elastischer Körper. J. für die reine und Angew. Math. (Crelle's Journal) 156–171. https://doi.org/10.1515/crll.1882.92.156

Heu, C., Berquand, A., Elie-Caille, C., Nicod, L., 2012. Glyphosate-induced stiffening of HaCaT

keratinocytes, a Peak Force Tapping study on living cells. J. Struct. Biol. 178, 1–7. https://doi.org/10.1016/j.jsb.2012.02.007

Huang, W., Restrepo, D., Jung, J.Y., Su, F.Y., Liu, Z., Ritchie, R.O., McKittrick, J., Zavattieri, P., Kisailus, D., 2019. Multiscale Toughening Mechanisms in Biological Materials and Bioinspired Designs. Adv. Mater. 31, 1–37. https://doi.org/10.1002/adma.201901561

Hutter, J.L., Bechhoefer, J., 1998. Calibration of atomic- force microscope tips. Rev. Sci. Instrum. 64, 1868. https://doi.org/10.1063/1.1143970

Jimenez-Palomar, I., Shipov, A., Shahar, R., Barber, A.H., 2012. Influence of SEM vacuum on bone micromechanics using in situ AFM. J. Mech. Behav. Biomed. Mater. 5, 149–155. https://doi.org/10.1016/j.jmbbm.2011.08.018

Johnson, K.L., Kendall, K., Roberts, A.D., 1971. Surface Energy and the Contact of Elastic Solids. Proc. R. Soc. A Math. Phys. Eng. Sci. 324, 301–313. https://doi.org/10.1098/rspa.1971.0141

Kindt, J.H., Thurner, P.J., Lauer, M.E., Bosma, B.L., Schitter, G., Fantner, G.E., Izumi, M., Weaver, J.C., Morse, D.E., Hansma, P.K., 2007. In situ observation of fluoride-ion-induced hydroxyapatite–collagen detachment on bone fracture surfaces by atomic force microscopy. Nanotechnology 18, 135102. https://doi.org/10.1088/0957-4484/18/13/135102

Knapp, H.F., Stemmer, A., Reilly, G.C., Niederer, P., Tate, M.L.K., 2002. Development of preparation methods for and insights obtained from atomic force microscopy of fluid spaces in cortical bone. Scanning 24, 25–33. https://doi.org/10.1002/sca.4950240104

Kwok, J., Grogan, S., Meckes, B., Arce, F., Lal, R., D'Lima, D., 2014. Atomic force microscopy

reveals age-dependent changes in nanomechanical properties of the extracellular matrix of native human menisci: implications for joint degeneration and osteoarthritis. Nanomedicine Nanotechnology, Biol. Med. 10, 1777–1785. https://doi.org/10.1016/j.nano.2014.06.010

Lantz, M.A., O'Shea, S.J., Welland, M.E., Johnson, K.L., 1997. Atomic-force-microscope study of contact area and friction on $NbSe_2$. Phys. Rev. B 55, 10776–10785. https://doi.org/10.1103/PhysRevB.55.10776

Li, Q., Doyran, B., Gamer, L.W., Lu, X.L., Qin, L., Ortiz, C., Grodzinsky, A.J., Rosen, V., Han, L., 2015. Biomechanical properties of murine meniscus surface via AFM-based nanoindentation. J. Biomech. 48, 1364–1370. https://doi.org/10.1016/j.jbiomech.2015.02.064

Lin, Y., Xu, S., 2011. AFM analysis of the lacunar-canalicular network in demineralized compact bone. J. Microsc. 241, 291–302. https://doi.org/10.1111/j.1365-2818.2010.03431.x

Lozano, P.F., Scholze, M., Babian, C., Scheidt, H., Vielmuth, F., Waschke, J., Ondruschka, B., Hammer, N., 2019. Water-content related alterations in macro and micro scale tendon biomechanics. Sci. Rep. 9, 1–12. https://doi.org/10.1038/s41598-019-44306-z

Marturano, J.E., Arena, J.D., Schiller, Z.A., Georgakoudi, I., Kuo, C.K., 2013. Characterization of mechanical and biochemical properties of developing embryonic tendon. Proc. Natl. Acad. Sci. U. S. A. 110, 6370–6375. https://doi.org/10.1073/pnas.1300135110

Maugis, D., 1992. Adhesion of spheres: The JKR-DMT transition using a dugdale model. J. Colloid Interface Sci. 150, 243–269. https://doi.org/10.1016/0021-9797(92)90285-T

Meza, L.R., Zelhofer, A.J., Clarke, N., Mateos, A.J., Kochmann, D.M., Greer, J.R., 2015.

Resilient 3D hierarchical architected metamaterials. Proc. Natl. Acad. Sci. 112, 11502–11507. https://doi.org/10.1073/pnas.1509120112

Milovanovic, P., Potocnik, J., Stoiljkovic, M., Djonic, D., Nikolic, S., Neskovic, O., Djuric, M., Rakocevic, Z., 2011. Nanostructure and mineral composition of trabecular bone in the lateral femoral neck: Implications for bone fragility in elderly women. Acta Biomater. 7, 3446–3451. https://doi.org/10.1016/j.actbio.2011.05.028

Oliver, W.C., Pharr, G.M., 1992. An improved technique for determining hardness and elastic modulus using load and displacement sensing indentation experiments. J. Mater. Res. 7, 1564–1583. https://doi.org/10.1557/JMR.1992.1564

Piétrement, O., Troyon, M., 2000. General equations describing elastic indentation depth and normal contact stiffness versus load. J. Colloid Interface Sci. 226, 166–171. https://doi.org/10.1006/jcis.2000.6808

Raspanti, M., Congiu, T., Guizzardi, S., 2001. Tapping-mode atomic force microscopy in fluid of hydrated extracellular matrix. Matrix Biol. 20, 601–604. https://doi.org/10.1016/S0945-053X(01)00174-3

Reilly, G.C., Knapp, H.F., Stemmer, A., Niederer, P., Knothe Tate, M.L., 2001. Investigation of the Morphology of the Lacunocanalicular System of Cortical Bone Using Atomic Force Microscopy. Ann. Biomed. Eng. 29, 1074–1081. https://doi.org/10.1114/1.1424910

Reznikov, N., Shahar, R., Weiner, S., 2014a. Bone hierarchical structure in three dimensions. Acta Biomater. 10, 3815–3826. https://doi.org/10.1016/j.actbio.2014.05.024

Reznikov, N., Shahar, R., Weiner, S., 2014b. Three-dimensional structure of human lamellar

bone: The presence of two different materials and new insights into the hierarchical organization. Bone 59, 93–104. https://doi.org/10.1016/j.bone.2013.10.023

Rho, J.-Y., Roy, M.E., Tsui, T.Y., Pharr, G.M., 1999. Elastic properties of microstructural components of human bone tissue as measured by nanoindentation. J. Biomed. Mater. Res. 45, 48–54. https://doi.org/10.1002/(SICI)1097-4636(199904)45:1<48::AID-JBM7>3.0.CO;2-5

Rho, J Y, Currey, J.D., Zioupos, P., Pharr, G.M., 2001. The anisotropic Young's modulus of equine secondary osteones and interstitial bone determined by nanoindentation. J. Exp. Biol. 204, 1775–81. https://doi.org/10.1242/jeb.204.10.1775

Rho, J. Y., Mishra, S.R., Chung, K., Bai, J., Pharr, G.M., 2001. Relationship Between Ultrastructure and the Nanoindentation Properties of Intramuscular Herring Bones. Ann. Biomed. Eng. 29, 1082–1088. https://doi.org/10.1114/1.1424913

Rho, J.Y., Pharr, G.M., 1999. Effects of drying on the mechanical properties of bovine femur measured by nanoindentation. J. Mater. Sci. Mater. Med. 10, 485–8. https://doi.org/10.1023/A:1008901109705

Rho, J.Y., Tsui, T.Y., Pharr, G.M., 1997. Elastic properties of human cortical and trabecular lamellar bone measured by nanoindentation. Biomaterials 18, 1325–1330. https://doi.org/10.1016/S0142-9612(97)00073-2

Rho, J.Y., Zioupos, P., Currey, J.D., Pharr, G.M., 1999. Variations in the individual thick lamellar properties within osteons by nanoindentation. Bone 25, 295–300. https://doi.org/10.1016/S8756-3282(99)00163-5

Rico, F., Su, C., Scheuring, S., 2011. Mechanical Mapping of Single Membrane Proteins at Submolecular Resolution. Nano Lett. 11, 3983–3986. https://doi.org/10.1021/nl202351t

Roddy, K.A., Kelly, G.M., van Es, M.H., Murphy, P., Prendergast, P.J., 2011. Dynamic patterns of mechanical stimulation co-localise with growth and cell proliferation during morphogenesis in the avian embryonic knee joint. J. Biomech. 44, 143–149. https://doi.org/10.1016/j.jbiomech.2010.08.039

Roy, M.E., Rho, J.Y., Tsui, T.Y., Evans, N.D., Pharr, G.M., 1999. Mechanical and morphological variation of the human lumbar vertebral cortical and trabecular bone. J Biomed Mater Res 44, 191–197. https://doi.org/10.1002/(SICI)1097-4636(199902)44:2<191::AID-JBM9>3.0.CO;2-G [pii]

Sarid, D., Coratger, R., Ajustron, F., Beauvillain, J., 1991. Scanning force microscopy - With Applications to Electric, Magnetic and Atomic Forces. Microsc. Microanal. Microstruct. 2, 649–649. https://doi.org/10.1051/MMM:0199100206064900

Sasaki, N., Tagami, A., Goto, T., Taniguchi, M., Nakata, M., Hikichi, K., 2002. Atomic force microscopic studies on the structure of bovine femoral cortical bone at the collagen fibril-mineral level. J. Mater. Sci. Mater. Med. 13, 333–337. https://doi.org/10.1023/A:1014079421895

Sasaki, T., Debari, K., Hasemi, M., 1993. Measurement of Howship's Resorption Lacunae by a Scanning Probe Microscope System. J. Electron Microsc. (Tokyo). 42, 356–359. https://doi.org/10.1093/oxfordjournals.jmicro.a051054

Sneddon, I.N., 1965. The relation between load and penetration in the axisymmetric boussinesq problem for a punch of arbitrary profile. Int. J. Eng. Sci. 3, 47–57.

https://doi.org/10.1016/0020-7225(65)90019-4

Stolz, M., Raiteri, R., Daniels, A.U., VanLandingham, M.R., Baschong, W., Aebi, U., 2004. Dynamic elastic modulus of porcine articular cartilage determined at two different levels of tissue organization by indentation-type atomic force microscopy. Biophys. J. 86, 3269–83. https://doi.org/10.1016/S0006-3495(04)74375-1

Su, C., Shi, J., Hu, Y., Hu, S., Ma, J., 2014. Method and apparatus of using peak force tapping mode to measure physical properties of a sample. US9291640B2.

Svensson, R.B., Hassenkam, T., Hansen, P., Peter Magnusson, S., 2010. Viscoelastic behavior of discrete human collagen fibrils. J. Mech. Behav. Biomed. Mater. 3, 112–115. https://doi.org/10.1016/j.jmbbm.2009.01.005

Syed Asif, S.A., Wahl, K.J., Colton, R.J., Warren, O.L., 2001. Quantitative imaging of nanoscale mechanical properties using hybrid nanoindentation and force modulation. J. Appl. Phys. 90, 1192–1200. https://doi.org/10.1063/1.1380218

Syed Asif, S.A.S., Wahl, K.J., Colton, R.J., 1999. Nanoindentation and contact stiffness measurement using force modulation with a capacitive load-displacement transducer. Rev. Sci. Instrum. 70, 2408–2413. https://doi.org/10.1063/1.1149769

Tai, K., Dao, M., Suresh, S., Palazoglu, A., Ortiz, C., 2007. Nanoscale heterogeneity promotes energy dissipation in bone. Nat. Mater. 6, 454–462. https://doi.org/10.1038/nmat1911

Tai, K., Qi, H.J., Ortiz, C., 2005. Effect of mineral content on the nanoindentation properties and nanoscale deformation mechanisms of bovine tibial cortical bone. J. Mater. Sci. Mater. Med. 16, 947–959. https://doi.org/10.1007/s10856-005-4429-9

Tao, N.J., Lindsay, S.M., Lees, S., 1992. Measuring the microelastic properties of biological material. Biophys. J. 63, 1165–1169. https://doi.org/10.1016/S0006-3495(92)81692-2

Thalhammer, S., Heckl, W.M., Zink, A., Nerlich, A.G., 2001. Atomic Force Microscopy for High Resolution Imaging of Collagen Fibrils—A New Technique to Investigate Collagen Structure in Historic Bone Tissues. J. Archaeol. Sci. 28, 1061–1068. https://doi.org/10.1006/jasc.2000.0644

Thompson, J.B., Kindt, J.H., Drake, B., Hansma, H.G., Morse, D.E., Hansma, P.K., 2001. Bone indentation recovery time correlates with bond reforming time. Nature 414, 773–776. https://doi.org/10.1038/414773a

Tong, W., Glimcher, M.J., Katz, J.L., Kuhn, L., Eppell, S.J., 2003. Size and shape of mineralites in young bovine bone measured by atomic force microscopy, in: Calcified Tissue International. Springer, pp. 592–598. https://doi.org/10.1007/s00223-002-1077-7

van der Rijt, J.A.J., van der Werf, K.O., Bennink, M.L., Dijkstra, P.J., Feijen, J., 2006. Micromechanical Testing of Individual Collagen Fibrils. Macromol. Biosci. 6, 697–702. https://doi.org/10.1002/mabi.200600063

Voss, A., Dietz, C., Stocker, A., Stark, R.W., 2015. Quantitative measurement of the mechanical properties of human antibodies with sub-10-nm resolution in a liquid environment. Nano Res. 8, 1987–1996. https://doi.org/10.1007/s12274-015-0710-5

Wallace, J.M., Erickson, B., Les, C.M., Orr, B.G., Banaszak Holl, M.M., 2010. Distribution of type I collagen morphologies in bone: Relation to estrogen depletion. Bone 46, 1349–1354. https://doi.org/10.1016/j.bone.2009.11.020

Wallace, J.M., Orr, B.G., Marini, J.C., Holl, M.M.B., 2011. Nanoscale morphology of Type I collagen is altered in the Brtl mouse model of Osteogenesis Imperfecta. J. Struct. Biol. 173, 146–152. https://doi.org/10.1016/j.jsb.2010.08.003

Wang, M., Peng, Z., 2015. Investigation of the nano-mechanical properties and surface topographies of wear particles and human knee cartilages. Wear 324–325, 74–79. https://doi.org/10.1016/J.WEAR.2014.11.033

Wegst, U.G.K., Bai, H., Saiz, E., Tomsia, A.P., Ritchie, R.O., 2015. Bioinspired structural materials. Nat. Mater. 14, 23–36. https://doi.org/10.1038/nmat4089

Wenger, M.P.E., Bozec, L., Horton, M.A., Mesquida, P., 2007. Mechanical Properties of Collagen Fibrils. Biophys. J. 93, 1255–1263. https://doi.org/10.1529/biophysj.106.103192

Wilusz, R.E., DeFrate, L.E., Guilak, F., 2012. Immunofluorescence-guided atomic force microscopy to measure the micromechanical properties of the pericellular matrix of porcine articular cartilage. J. R. Soc. Interface 9, 2997–3007. https://doi.org/10.1098/rsif.2012.0314

Wolff, J., 1986. The Law of Bone Remodelling, The Law of Bone Remodelling. https://doi.org/10.1007/978-3-642-71031-5

Xia, D., Zhang, S., Hjortdal, J.Ø., Li, Q., Thomsen, K., Chevallier, J., Besenbacher, F., Dong, M., 2014. Hydrated Human Corneal Stroma Revealed by Quantitative Dynamic Atomic Force Microscopy at Nanoscale. ACS Nano 8, 6873–6882. https://doi.org/10.1021/nn5015837

Xu, J., Rho, J.Y., Mishra, S.R., Fan, Z., 2003. Atomic force microscopy and nanoindentation characterization of human lamellar bone prepared by microtome sectioning and mechanical

polishing technique. J. Biomed. Mater. Res. A 67, 719–26. https://doi.org/10.1002/jbm.a.10109

Xue, Y., Wang, L., Xia, D., Li, Q., Gao, S., Dong, M., Cai, T., Shi, S., He, L., Hu, K., Mao, T., Duan, X., 2015. Dental Abnormalities Caused by Novel Compound Heterozygous CTSK Mutations. J. Dent. Res. 94, 674–681. https://doi.org/10.1177/0022034515573964

Yang, L., van der Werf, K.O., Fitié, C.F.C., Bennink, M.L., Dijkstra, P.J., Feijen, J., 2008. Mechanical Properties of Native and Cross-linked Type I Collagen Fibrils. Biophys. J. 94, 2204–2211. https://doi.org/10.1529/biophysj.107.111013

Yao, H., Dao, M., Carnelli, D., Tai, K., Ortiz, C., 2011. Size-dependent heterogeneity benefits the mechanical performance of bone. J. Mech. Phys. Solids 59, 64–74. https://doi.org/10.1016/j.jmps.2010.09.012

Zhang, C., Yan, B., Cui, Z., Cui, S., Zhang, T., Wang, X., Liu, D., Yang, R., Jiang, N., Zhou, Y., Liu, Y., 2017. Bone regeneration in minipigs by intrafibrillarly-mineralized collagen loaded with autologous periodontal ligament stem cells. Sci. Reports 2017 71 7, 1–9. https://doi.org/10.1038/s41598-017-11155-7

Zhang, S., Bach-Gansmo, F.L., Xia, D., Besenbacher, F., Birkedal, H., Dong, M., 2015. Nanostructure and mechanical properties of the osteocyte lacunar-canalicular network-associated bone matrix revealed by quantitative nanomechanical mapping. Nano Res. 8, 3250–3260. https://doi.org/10.1007/s12274-015-0825-8

Zhang, Y., Cui, F.., Wang, X.., Feng, Q.., Zhu, X.., 2002. Mechanical properties of skeletal bone in gene-mutated stöpseldtl28d and wild-type zebrafish (Danio rerio) measured by atomic force microscopy-based nanoindentation. Bone 30, 541–546. https://doi.org/10.1016/S8756-

3282(02)00676-2

Zhong, Q., Inniss, D., Kjoller, K., Elings, V.B., 1993. Fractured polymer/silica fiber surface studied by tapping mode atomic force microscopy. Surf. Sci. Lett. 290, L688–L692. https://doi.org/10.1016/0167-2584(93)90906-Y

Zhou, Y., Kastner, M.J., Tighe, T.B., Du, J., 2020. Elastic modulus mapping for bovine cortical bone from submillimeter- to submicron-scales using PeakForce Tapping atomic force microscopy. Extrem. Mech. Lett. 41, 101031. https://doi.org/10.1016/j.eml.2020.101031

1 **Tables**

2 Table 1. Elastic modulus of bone and components in bone measured using various AFM methods

| Specimen | Testing Condition | Experimental Method | Probe | Loading Profile | Mechanics Theories and Models | Elastic Modulus (GPa) | Reference |
|---|---|---|---|---|---|---|---|
| Bovine tibia | Under water or saline | AFM contact indentation mode | Pyramidal corner; Silicon nitride | Penetration depth 3 – 50 nm; Maximum load of 2.5 and 205 nN | Sneddon; Cones with semivertical angle of 72° | Osteonal lamella, 0.7–0.9 (shear modulus); Interstitial lamella, 0.06–0.13 (shear modulus). | (Tao et al., 1992) |
| Osteoblast cell culture | In cell culture medium, 37°C and 5% $CO_2$ | AFM force mapping (contact indentation) | Cantilever spring constant 8 mN/m | 7.1 curves per second for 32 force curves per line; 12 force curves per second for 64 force curves per line; Trigger threshold of 110 nm. | Sneddon | Osteoclast, 8.8 kPa on Ti substrate; Osteoclast, 2.1 kPa on TiV substrate. | (Domke et al., 2000) |
| Human femur | Dry/Immersed in Ringer solution | Nanoindenter + AFM controller | Berkovich | Maximum load of 0.2 - 5 mN | Oliver-Pharr | Osteonal thick sub-lamella, dry 23.8–17.1, wet, 19.8–9.5; Osteonal thin sub-lamella, dry 20.5–16.8, wet 17.1–11.6; Trabecular thick sub-lamella, dry 27.2–20.2, wet 18.3–10.8; Trabecular thin sub-lamella, dry 24.8–21.9, wet 20.5–8.1. | (Hengsberger et al., 2002) |
| Human femur | Dry | Nanoindenter + AFM controller | Berkovich | Loading/ unloading rate of 300 μN/s; Maximum load of 1.5 mN | Oliver-Pharr | Osteonal thick sub-lamella, polished 23.28 ± 2.20, microtomed 24.36 ± 2.86; Osteonal thin sub-lamella, polished 21.94 ± 2.66, microtomed 20.34 ± 1.88. | (Xu et al., 2003) |
| Bovine tibia | Dry | Nanoindenter + AFM controller | Berkovich | Loading/unloading rate of 9 μN/s; Maximum load 100-1000 μN; Holding 10-20 s | Oliver-Pharr and FEA | EDTA-demineralized cortical bone: Mineral content 58 wt%, 12.9 ± 2.9; Mineral content, 37 wt%, 7.9 ± 2.7; Mineral content, 26 wt%, 3.0 ± 0.5; Mineral content, 4 wt%, 3.8 ± 0.7; Mineral content, 0 wt%, 1.9 ± 0.1. | (Tai et al., 2005) |

| | | | | | | | |
|---|---|---|---|---|---|---|---|
| Mouse mid-tibial cortical bone | Dry | Nanoindenter + AFM controller | N/A | Nanoindentation with maximum load of 300 – 600 μN | Oliver-Pharr | Wild type, ~ 20.4;<br>DNTβRII mice with reduced TGF-β signaling, increased by 33%;<br>Smad3 mice with impaired TGF-β signaling, increased by 42%. | (Balooch et al., 2005) |
| | | | | Sinusoidal modulated force of 3 μN | (Syed Asif et al., 2001, 1999) | Elastic map:<br>Homogeneous in wild type, ~32;<br>Heterogeneity in D4 phenotypes, 15 – 40. | |
| Rabbit femoral condyle | Dry | Nanoindenter + AFM controller | Berkovich | Loading/unloading rate of 50 μN/s; Maximum load from 250 to 3000 μN; Holding for 10 s | Oliver-Pharr | For shallow indentations,<br>Trabecular thick lamella, 26.6 ± 2.27;<br>Trabecular thin lamella, 20.3 ± 2.09.<br>For large indentations,<br>Trabecular thick and thin lamella, ~20. | (Donnelly et al., 2006) |
| Bovine cortical bone | Dry | AFM contact indentation mode | Tetrahedral silicon cantilever; Spring constant 56.2 N/m; Tip radius ~ 15 nm. | Maximum load of 5 μN; 100 nm spacing | Oliver-Pharr and FEA | Osteon longitudinal, 12.9 ± 4.8;<br>Osteon transverse, 8.55 ± 3.7. | (Tai et al., 2007) |
| Bovine cortical bone | Dry | AFM contact indentation mode | Same as (Tai et al., 2007) | Same as (Tai et al., 2007) | Oliver-Pharr | Results from AFM contact indentation mode:<br>Osteon longitudinal, 6 – 30;<br>Osteon transverse, 4 – 15.<br>Combining with results from nanoindentation:<br>Heterogeneity below length scale 200 nm. | (Yao et al., 2011) |
| | | Nanoindentation | Berkovich | Displacement control; Maximum depths 50, 100, 200, 300 nm. | | | |
| Rat femur | Rehydrated in HBSS vapor. High/low vacuum; wet in air. | AFM bending, *in situ* SEM | AFM cantilever spring constant 28 N/m; FIB flattened tip. | Loading rate 0.2 μm/s | Beam bending theory | High vacuum 4.98 ± 0.25; Low vacuum 5.24 ± 0.11; Wet in air 5.22 ± 0.15. | (Jimenez-Palomar et al., 2012). |
| Bovine tibia | Fresh, ambient | Nanoindentation + AFM scans | Berkovich | Loading rate 20 nm/s; Unloading rate 100 nm/s; Maximum depths 50, 100, 200, 300 | Oliver-Pharr | Osteon longitudinal, oscillation from 26.24 ± 1.68 to 19.73 ± 0.73;<br>Osteon transverse, oscillation from 23.59 ± 3.55 to 15.39 ± 1.04. | (Carnelli et al., 2013) |

| | | | | | | | |
|---|---|---|---|---|---|---|---|
| | | | | nm; Spacing 0.5, 1, 2, 3 μm | | | |
| Rat mid-femur cortical | Dry | Nanoindentation | Berkovich | 10 s loading, 60 s holding, 10 s unloading; Maximum load 500 μN; 1 μm spacing | Oliver-Pharr | Heterogeneity in the elastic map near a lacuna, ~4 – ~50; | (Zhang et al., 2015) |
| | | AFM PeakForce QNM | Etched silicon probe; Tip radius 8 nm; Spring constant 200 N/m | Maximum force 250 – 350 nN | N/A | Perilacunar matrix, 10.0 ± 2.8; bone matrix, 28.8 ± 10.1.<br>Pericanalicular matrix, 20.0 ± 7.5; bone matrix, 31.6 ± 5.2.<br>Collagen fiber in perilacunar matrix, 12.6 ± 3.5. | |
| Minipig cranial bone | Ambient | AFM PeakForce QNM | N/A | N/A | N/A | Natural bone, 7.5 ± 0.6;<br>Newly-formed bone in defect treated with IMC scaffolds, 5.1 ± 0.7;<br>Newly-formed bone in defect treated with HA scaffolds, 3.6 ± 0.8. | (Zhang et al., 2017) |
| Mouse femur | Dry | AFM contact indentation | Non-contact high resonance cantilevers; Spring constant 40 N/m; Spherical tips radii 50, 100, 300 nm; Resonance frequency 330 kHz; Length 125 μm | Indentation frequency between 1 and 500 Hz; Scan size 30 μm; 64 × 64, 128 × 128, or 256 × 256 pixels | Hertzian | Cortical metaphysis, longitudinal 1.64± 0.31, transverse 1.33± 0.37;<br>Cortical mid-diaphysis, longitudinal 1.90± 0.31, transverse 1.54± 0.21;<br>Trabecula femoral head, longitudinal 0.93± 0.20, transverse 0.54± 0.29;<br>Trabecula distal epiphysis, longitudinal 0.83± 0.31, transverse 0.47± 0.18;<br>Trabecula metaphysis, longitudinal 0.84± 0.29, transverse 0.43± 0.15. | (Asgari et al., 2019) |
| Bovine cortical femur | Immersed in DI water | AFM PeakForce QNM | Etched silicon probe; Tip radius 8 nm; Spring constant 200 N/m | Maximum force 400 nN; 1 kHz force frequency; 0.5 Hz scan rate; Scan size 100, 11, 6.6 μm; 256 × 256 pixels | DMT | Osteons, 20.51 ± 6.85;<br>Interstitial bone, 21.87 ± 5.48;<br>Thick sub-lamella, 21.49 ± 6.58;<br>Thin sub-lamella, 9.67 ± 2.69;<br>Cement line, 7.49 ± 4.23;<br>Mineralized collagen fibril bundle, 12.94 ± 2.71GPa;<br>Extrafibrillar matrix, 28.39 ± 5.75. | (Zhou et al., 2020) |

1

**List of Figures**

distance, *r*, begins at the edge of the Haversian canal. Dashed lines show the results of fitting experimental data to an oscillatory function. Adapted from (Carnelli et al., 2013).

Figure 6. (a) Height image of a living osteoblast recorded in contact mode. The white box indicates the area shown in (b). (b) Elastic modulus map of the boxed section in the osteoblast in (a). (adapted from (Domke et al., 2000))

Figure 7. Typical elastic modulus maps of bovine compact bone in ambient conditions obtained from indentations using AFM probes and Oliver-Pharr method with the indentation direction (a) parallel to the long bone axis (axial loading) and (b) perpendicular to the long bone axis (transverse loading), respectively. (Adapted from (Yao et al., 2011))

Figure 8. (a) AFM image of a fractured surface of human trabecular bone showing filaments (arrows) between neighboring fibrils (scale bar: 200 nm) (Fantner et al., 2005); (b) A representative tension curve obtained during the AFM force measurement on a piece of bone with another piece of bone glued to the AFM cantilever probe (adapted from (Fantner et al., 2005)); (c) Electron micrograph of a collagen fibril attached with one glue droplet to the substrate (down right) and a second droplet to the AFM cantilever (top left) (van der Rijt et al., 2006); (d) Two representative loading-unloading stress-strain curves obtained from the tension test of single collagen fibrils using AFM at ambient conditions (van der Rijt et al., 2006).

Figure 9. Surface morphology and reduced elastic modulus map for the lacunar-canalicular network surrounding osteocytes measured using PeakForce AFM. (a) Surface morphology and (b) reduced elastic modulus map of the bone surrounding an osteocyte lacuna (noted by L in the figures); (c) Histograms of the reduced modulus for perilacunar matrix and bone matrix (boxed areas in (a) and (b)). (d) Surface morphology and (e) reduced elastic modulus map of the bone

surrounding a canaliculus (noted by C in the figures); (f) Histograms of the reduced modulus for pericanalicular matrix and bone matrix. (g) Surface morphology and (h) reduced modulus map of collagen fibrils in the perilacunar matrix near an osteocyte lacuna; (j) Histograms of the reduced elastic modulus for the collagen fibrils and bone matrix. (adapted from (Zhang et al., 2015))

Figure 10. (a) Elastic modulus map of alternating thick and thin sub-lamellae in an osteon; Histograms of elastic modulus for (b) thick sub-lamellae and (c) thin sub-lamellae, respectively. Elastic modulus map of (d) mineralized collagen fibril bundles (dashed ellipse) and extrafibrillar matrix and (e) bundle-matrix patterns in the interstitial bone, which was not shown in the cement line; Histograms of elastic modulus for (f) mineralized collagen fibril bundles and (g) extrafibrillar matrix. (adapted from (Zhou et al., 2020))

Figure1

Click here to access/download;Figure;Figure1.tif

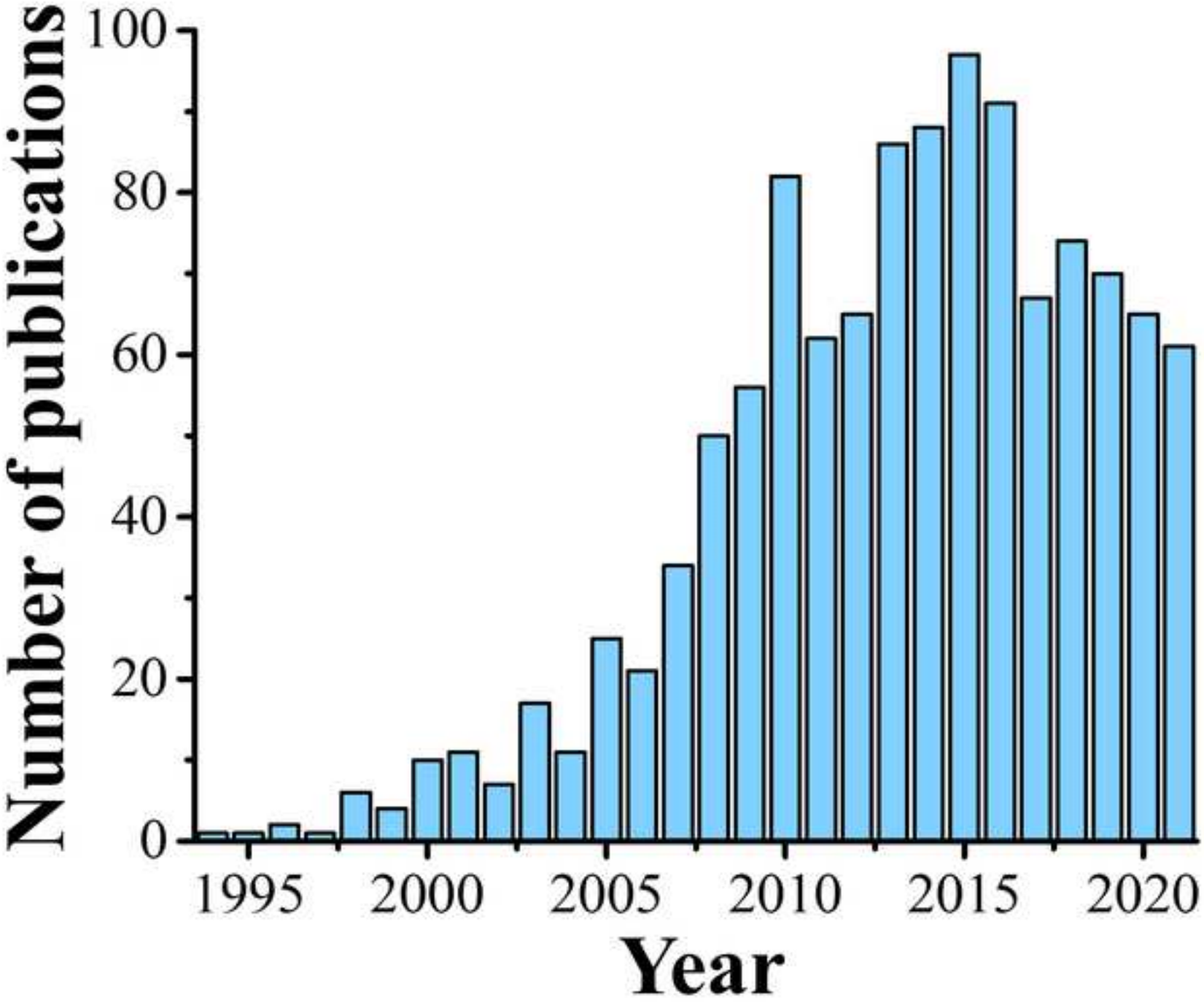

Figure 2



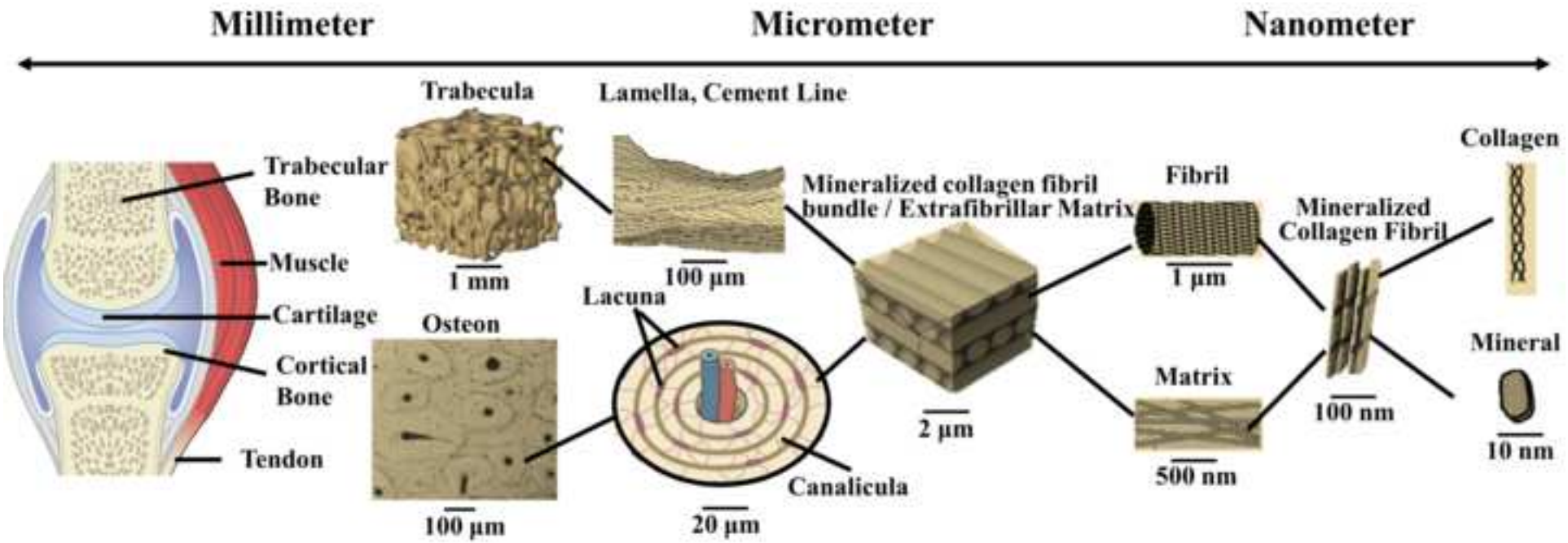

Figure 3



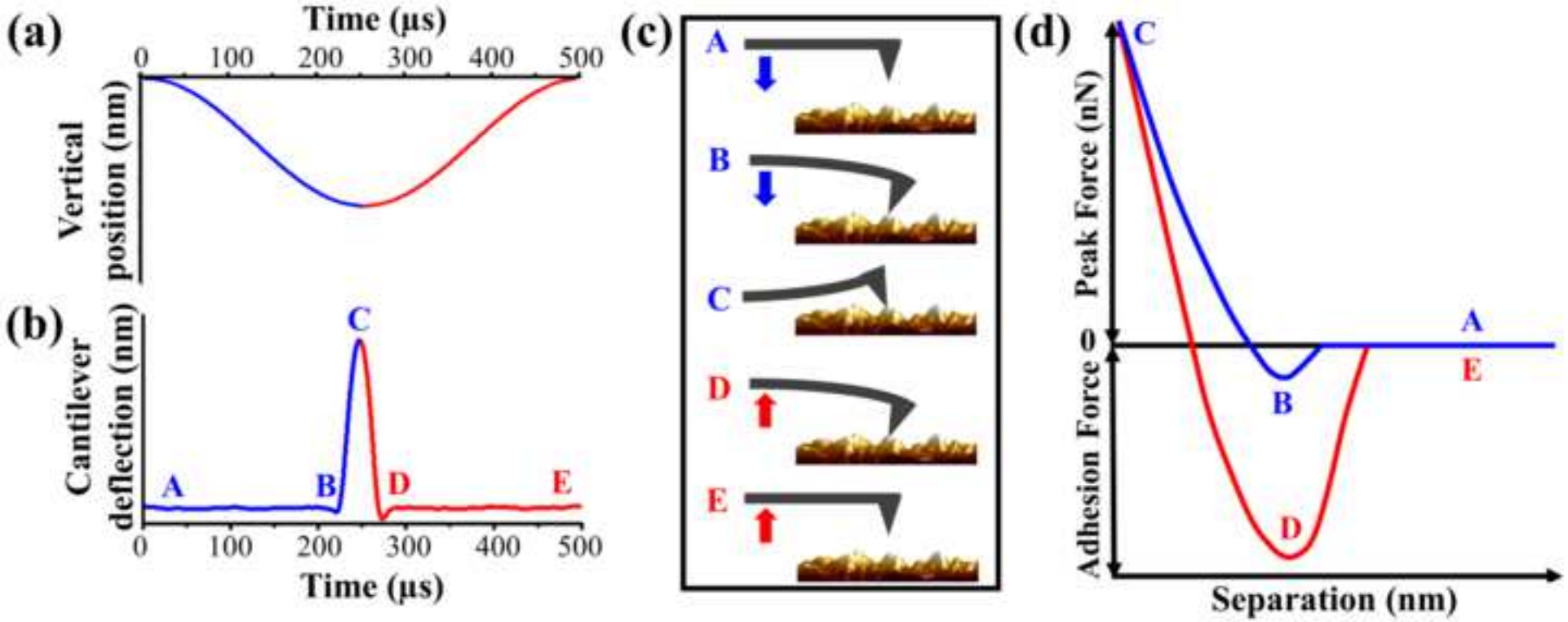

Figure 4



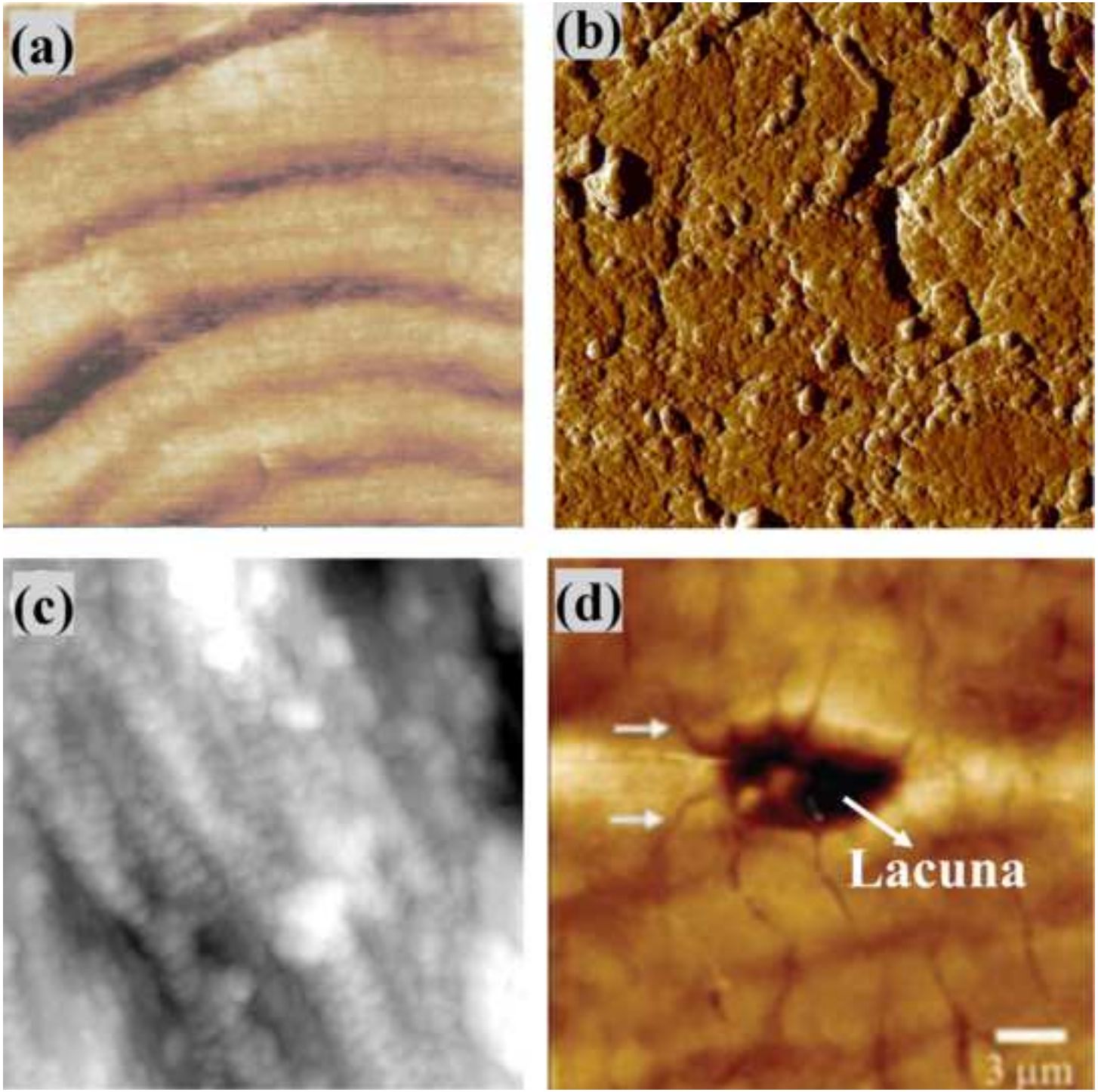

Figure 5



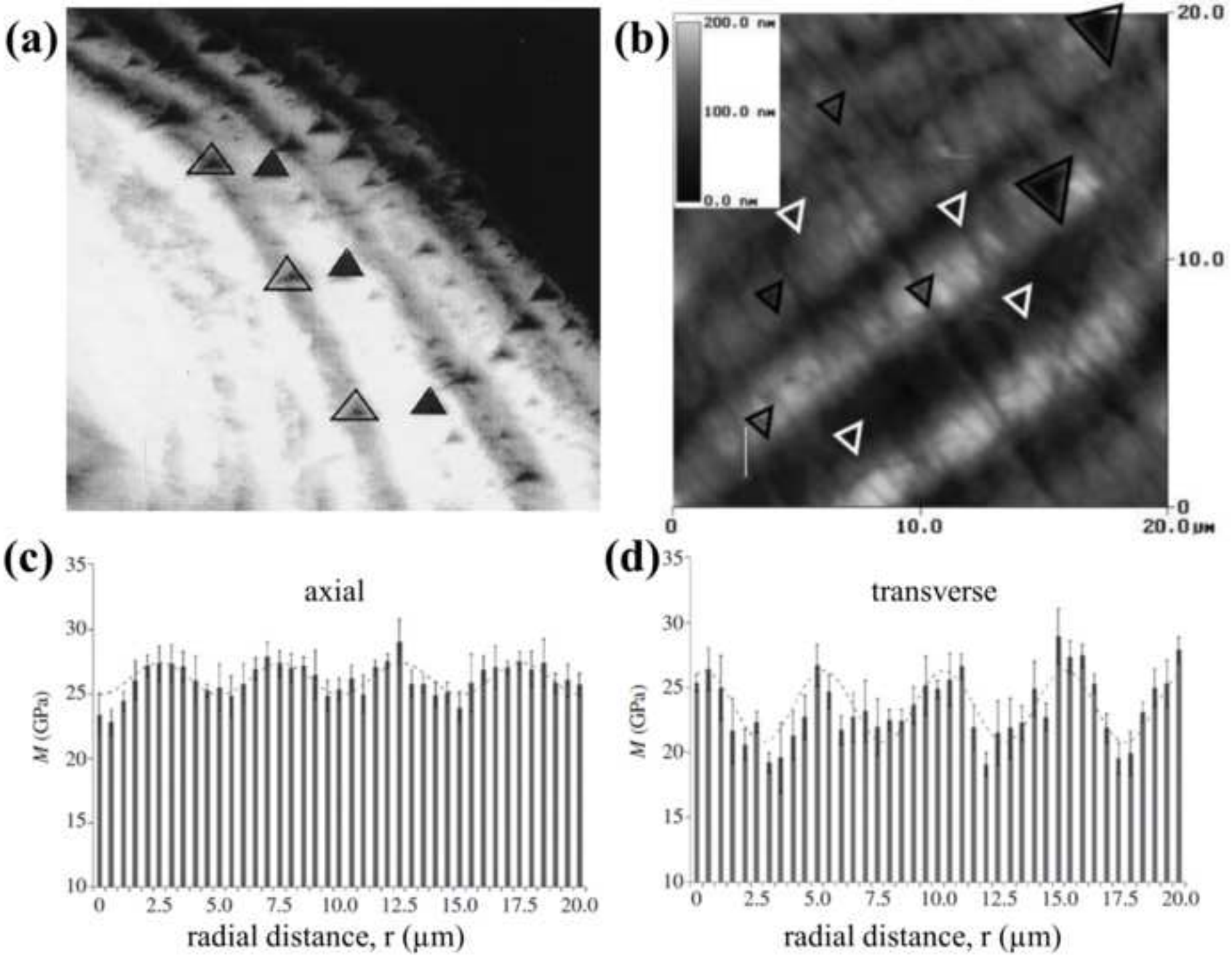

Figure 6



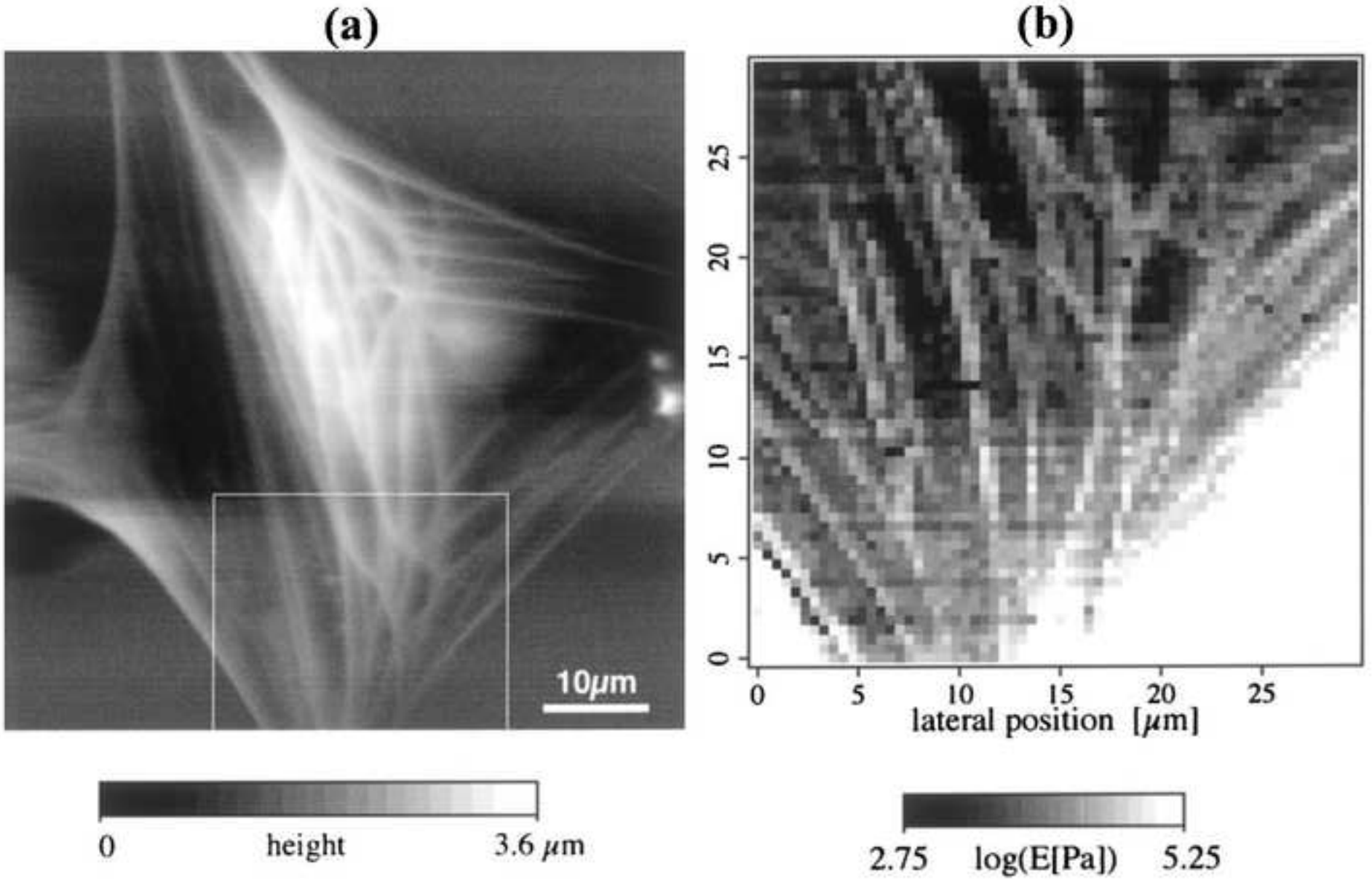

Figure7



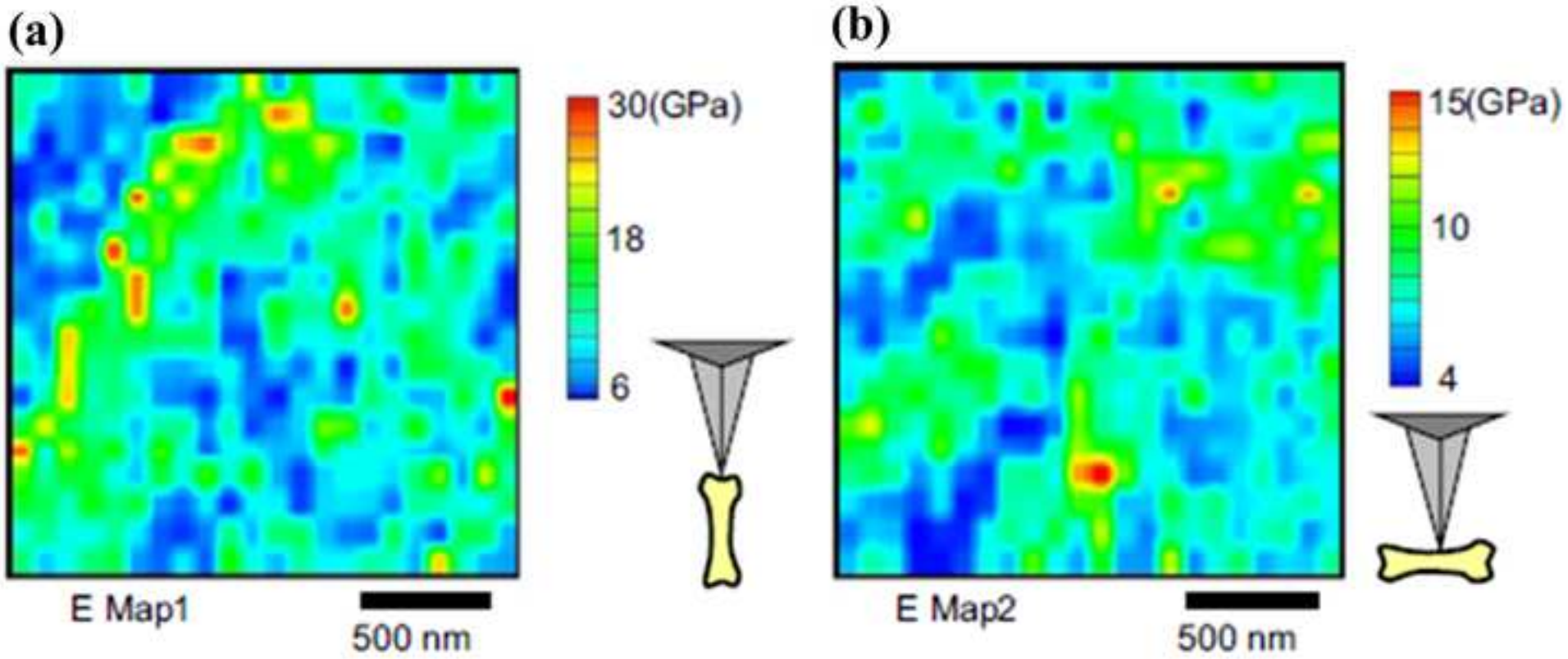

Figure 8



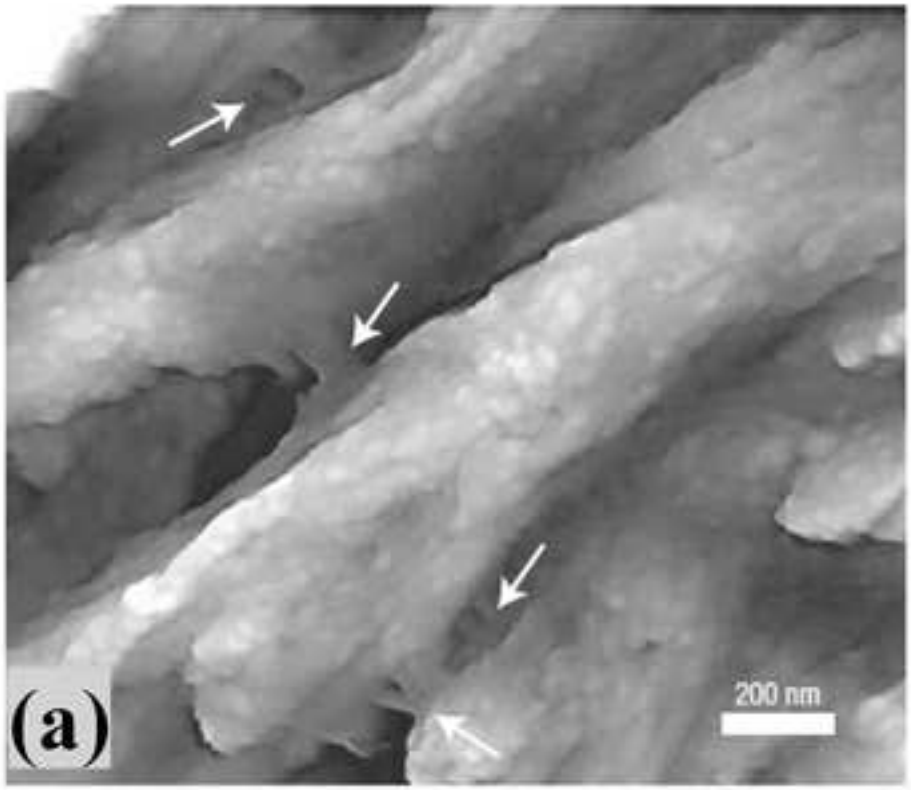


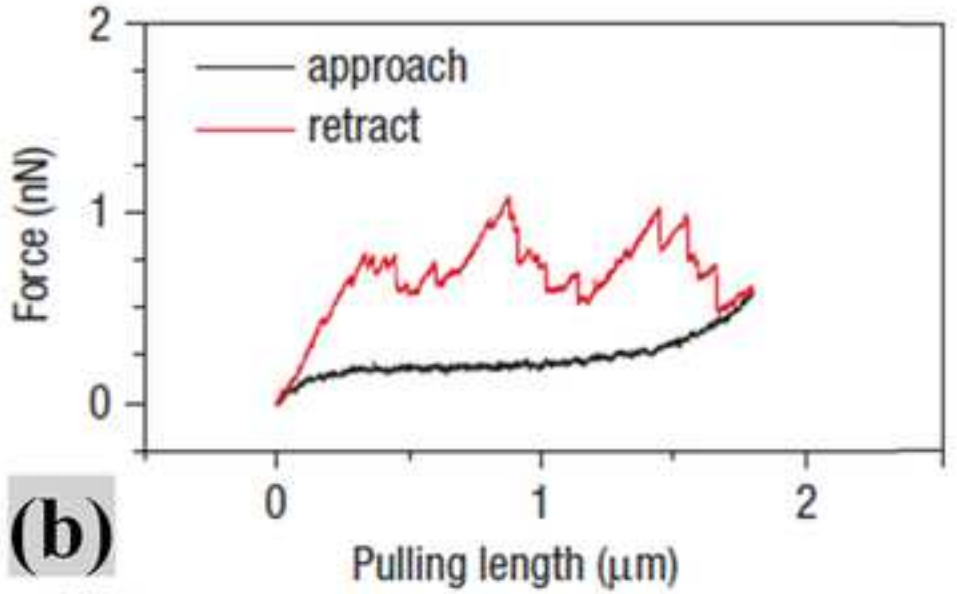


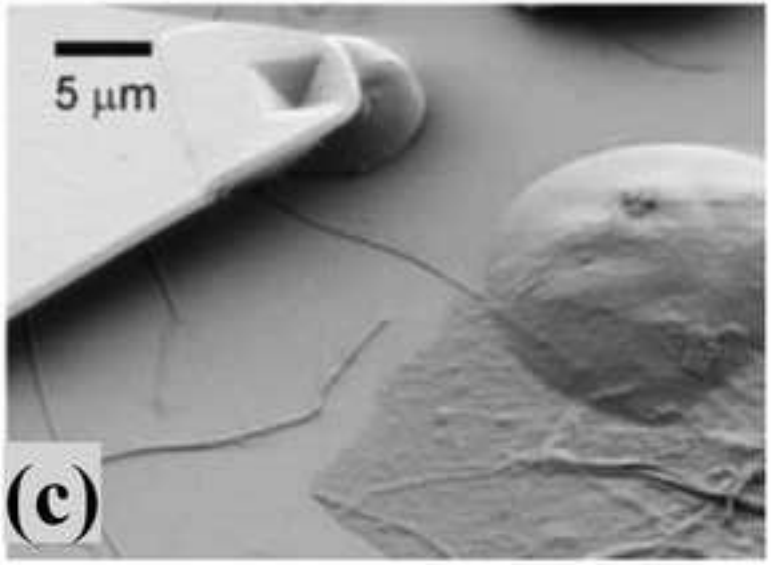


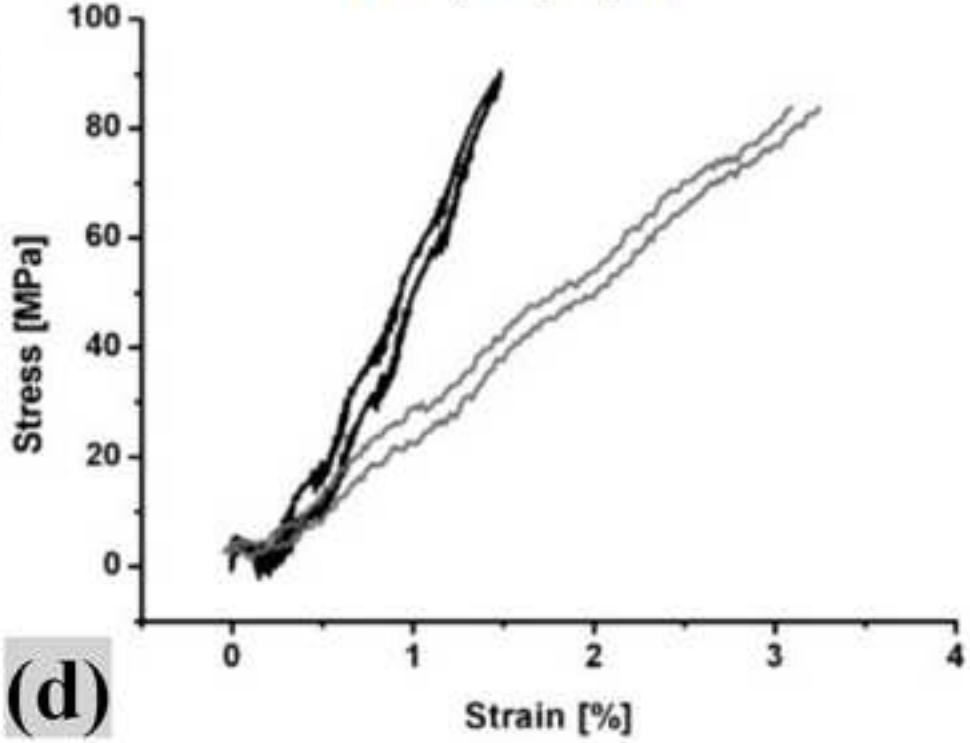

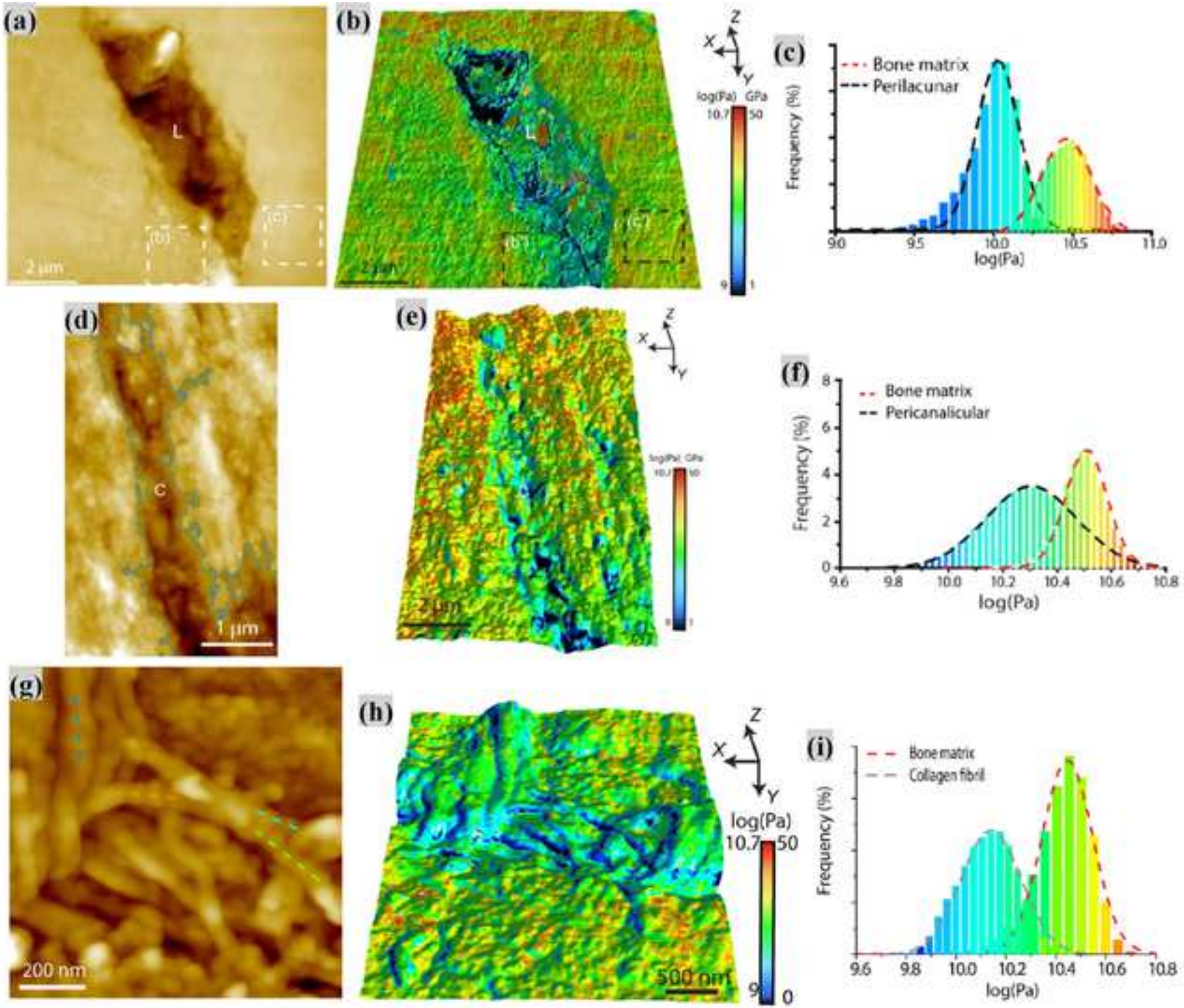

Figure10 Click here to access/download;Figure;Figure10.tif